The Dynamics of Dense Cores in the Perseus Molecular Cloud II: the Relationship between Dense Cores and the Cloud

The Dynamics of Dense Cores in the Perseus Molecular Cloud II: The Relationship Between Dense Cores and the Cloud

Helen Kirk[1,2,3], Jaime E. Pineda[4], Doug Johnstone[2,1], and Alyssa Goodman[4]

ABSTRACT

We utilize the extensive datasets available for the Perseus molecular cloud to analyze the relationship between the kinematics of small-scale dense cores and the larger structures in which they are embedded. The kinematic measures presented here can be used in conjunction with those discussed in our previous work as strong observational constraints that numerical simulations (or analytic models) of star formation should match. We find that dense cores have small motions with respect to the ^{13}CO gas, about one third of the ^{13}CO velocity dispersion along the same line of sight. Within each extinction region, the core-to-core velocity dispersion is about half of the total (^{13}CO) velocity dispersion seen in the region. Large-scale velocity gradients account for roughly half of the total velocity dispersion in each region, similar to what is predicted from large-scale turbulent modes following a power spectrum of $P(k) \propto k^{-4}$.

1. INTRODUCTION

Star formation research is entering an era where the properties of dense, star-forming cores and their environs can be described in a statistical manner across many molecular cloud environments. Existing multi-cloud surveys include the COMPLETE Survey (Ridge et al. 2006), *Spitzer* c2d Survey (Evans et al. 2003), and *Spitzer* Gould Belt Surveys, while surveys that are in progress include the JCMT and *Herschel* Gould Belt surveys (Ward-Thompson et al. 2007; André & Saraceno 2005). These surveys will characterize dense core properties with sufficient detail to allow for the measurement of both global

[1]Department of Physics & Astronomy, University of Victoria, Victoria, BC, V8P 1A1, Canada

[2]National Research Council of Canada, Herzberg Institute of Astrophysics, 5071 West Saanich Road, Victoria, BC, V9E 2E7, Canada

[3]Currently at Harvard-Smithsonian Center for Astrophysics; hkirk@cfa.harvard.edu

[4]Harvard-Smithsonian Center for Astrophysics, 60 Garden St, Cambridge, MA 02138, USA

properties as well as the variation due to molecular cloud environment. Numerical simulations have also begun to make explicit predictions about a variety of observable dense core properties, going beyond global statistics such as the mass function.

One nearby molecular cloud that has been particularly well-studied already is Perseus. The Perseus molecular cloud is located relatively close-by at a distance of 250 pc (Černis 1993) and is an intermediate-mass star-forming region with protostars and dense cores found primarily within small clustered environments (e.g., NGC 1333 and IC 348). To study the dense cores in an unbiassed manner, dust column density observations have been undertaken in the (sub)millimetre continuum (Hatchell et al. 2005; Kirk, Johnstone, & Di Francesco 2006, hereafter KJD06; Enoch et al. 2006) and the large-scale structure of the cloud has been determined through extinction inferred via reddening of stars in the 2MASS dataset (KJD06; Ridge et al. 2006). The young protostellar content of the cloud has been measured using *Spitzer* data (Rebull et al. 2007; Jørgensen et al. 2007; Hatchell et al. 2007a). Molecular line data also exist on multiple scales within the cloud. The kinematics of the dense cores have been traced by pointed observations of N_2H^+ (Kirk, Johnstone & Tafalla 2007, hereafter KJT07) and NH_3 (Rosolowsky et al. 2008), and their immediate less-dense surroundings in $C^{18}O$ (KJT07) and CCS (Rosolowsky et al. 2008). Note that carbon-bearing molecules tend to freeze out quickly onto dust grains in the centres of cold, dense cores, while the absence of CO molecules leads to an enhanced production of nitrogen-bearing molecules (see, for example, Tafalla et al. 2002). Hence in dense cores, nitrogen-based molecules tend to trace the dense parts of the cores, while carbon-bearing molecules tend to trace the lower density envelopes of the cores. The less-dense gas in Perseus has been mapped in its entirety at lower resolution in ^{12}CO(1–0) and ^{13}CO(1–0) (Ridge et al. 2006; Pineda et al. 2008), with outflows identified across the entire cloud in an unbiassed manner using the ^{12}CO(1–0) dataset (Arce et al 2010), and outflows around the dense cores mapped in ^{12}CO(3–2) (Hatchell et al. 2007b).

Since a wealth of data exist for the Perseus molecular cloud, it is possible to move beyond characterizing properties of structures in the cloud based on a single tracer, and advance to a study of the kinematic relationship between the structures on different scales within the cloud.

Several studies have already been carried out which compare the column density features on various scales in Perseus. Jørgensen et al. (2007) related the young embedded protostars to the SCUBA dense cores that they inhabit and showed that the protostars have little, if any, motion within the dense core they form out of. In turn, the SCUBA dense cores are found only within high extinction zones within the molecular cloud, suggesting an extinction threshold of $A_V \sim 5$ mag for dense core formation (KJD06). Such a threshold is consis-

tent with predictions from a magnetically-dominated formation scenario, wherein dense core formation is only possible in the highest column density regions, where the ionization fraction is low enough to allow for a fast ambipolar diffusion timescale (McKee 1989). The dense cores also tend to be offset from the peaks of the larger extinction regions that they inhabit in a pattern suggestive of a triggered formation scenario (KJD06). A nearby B0 star, 40 Persei, previously suggested as a trigger for star formation in the nearby L1451 region (Walawender et al. 2004), is located in a position to be consistent with this scenario (KJD06).

A multi-scale analysis of kinematics comparable to the column density studies has not yet been performed, although the previous single-scale analyses reveal information which already places constraints on the star formation scenario. The pointed N_2H^+(1–0) and $C^{18}O$(2–1) observations (KJT07) of the dense cores showed that the dense cores in Perseus are intimately tied to their surrounding envelope of material. The velocity dispersion of each core's N_2H^+ gas tends to be thermally-dominated, while the velocity dispersion of each core's surrounding $C^{18}O$ gas tends to be much more non-thermal. Despite this, the difference in centroid velocities between the N_2H^+ and $C^{18}O$ gas is typically less than the sound speed, and much less than the velocity dispersion of the $C^{18}O$ gas. Similar results were found from the pointed NH_3(1,1) and (2,2) and CCS(2–1) survey (Rosolowsky et al. 2008). In Perseus, N_2H^+ and NH_3 have been shown to trace each other very well (Johnstone et al. 2010).

In a survey of isolated dense cores in a variety of star-forming regions, Walsh et al. (2004) found similarly small velocity differences and argued that this is evidence against the competitive accretion scenario. Ayliffe et al. (2007) analyzed a simulation where cores undergo competitive accretion and produced mock observations to match the Walsh et al. (2004) survey. Ayliffe et al. (2007) found they could match the small velocity differences at later times in the simulation, however, the dense core line width at later times greatly exceeded that found in observations. This illustrates that 'observations' of simulations are necessary for comparisons, as they can produce unexpected results. The Perseus observations of KJT07 extend the result of small centroid velocity differences to a more clustered star formation environment, where competitive accretion is predicted to be more effective (see, for example, Ayliffe et al. 2007).

Using estimates of the mass and size of the dense cores from the SCUBA observations and the internal velocity dispersion from the N_2H^+ survey, KJT07 furthermore showed that each dense core appears to be in approximate "virial equilibrium", so long as the surface pressure on the cores (from the overlying mass of the cloud) is considered.

Simulators have started to 'observe' similar kinematic measures in their simulations, such as the internal velocity dispersion of cores (Klessen et al. 2005; Ayliffe et al. 2007; Offner

et al. 2008; Kirk, Johnstone, & Basu 2009, hereafter KJB09) and the core-to-envelope velocity difference (Ayliffe et al. 2007; KJB09). These measurements allow for a direct comparison between the observational kinematic surveys and the simulations. In this paper, we use the multi-scale kinematic data available in the Perseus molecular cloud to provide further observational measures by which to test future models of star formation. In the interest of facilitating the comparison between observations and simulations, we focus on physically-motivated quantities that are simple to derive. It is hoped that these simple observational measures can be related to simulations without many additional assumptions required for the simulations.

In Section 2, we summarize the observational data used in our analysis, while in Sections 3-6, we present results based on small- (Section 3) to large- (Sections 5 and 6) scale quantities. Interpretation of the results is discussed in Section 7, and we conclude in Section 8. A glossary of the kinematic measures used in this paper is provided in Appendix A.

2. OBSERVATIONS

Our analysis here is based primarily on two datasets - a pointed survey of the kinematics of the dense cores (N_2H^+) and their surrounding material ($C^{18}O$) in Perseus (KJT07), and a survey of the less-dense gas (^{13}CO) spanning the entire Perseus cloud (Ridge et al. 2006; Pineda et al. 2008). Additionally, we make use of the large structures (termed 'extinction regions' in this paper) identified in an extinction map of Perseus based on analysis of the 2MASS dataset ('extinction super cores' in KJD06). Here, we summarize the relevant information for each of these datasets.

2.1. Pointed N_2H^+ and $C^{18}O$ Observations

Using the IRAM 30 m telescope, KJT07 made single pointing observations in frequency-switching mode of N_2H^+(1–0) and $C^{18}O$(2–1) in 157 candidate dense cores in Perseus. The beamsize was $25''$ for N_2H^+ and $11''$ for $C^{18}O$. The positions observed were selected primarily based on the SCUBA submillimetre analysis of KJD06, with additional targets selected based on a visual inspection of the Palomar plates and the location of the maxima of large-scale structures seen in the 2MASS-based extinction map of Perseus (KJD06). N_2H^+ emission was detected in the majority of pointings (97), with the highest fraction of detections belonging to the SCUBA dense core list (84%) and lower fractions (42% and 14% respectively) for the others. $C^{18}O$ emission was detected in all but one of the pointings. Linewidths, centroid

velocities, and integrated intensities were measured for all of the spectra with detected signal. N_2H^+(1–0) has seven hyperfine components in its spectrum and these were simultaneously fit using CLASS's hyperfine fitting program. The vast majority of the N_2H^+ spectra required a single velocity fit, and of the few cases where a second velocity component was required, the two components were usually discernible in the spectrum. The $C^{18}O$ spectra were fit with a single Gaussian where appropriate, but more frequently required a two-component Gaussian fit. Table 1 summarizes the relevant results used in this analysis: the difference in centroid velocities, $v_{N2H+} - v_{C18O}$, and the linewidth (one sigma of a Gaussian fit) of the $C^{18}O$, σ_{C18O}, for every N_2H^+ detection[1]. See Tables 3 and 4 in KJT07 for the full spectral fit parameters for N_2H^+ and $C^{18}O$ respectively. Note that when N_2H^+ spectra are plotted in this paper, the single Gaussian profile derived from the model fit is shown for simplicity.

The dense cores were further divided into protostellar and starless, based on associations with the Perseus embedded YSO catalog of Jørgensen et al. (2007). This YSO catalog uses two criteria of which protostars must satisfy at least one. The first criterion is the spatial coincidence of a *Spitzer* source and a SCUBA core, and the second criterion is colours that satisfy [3.6] - [4.5] > 1 and [8.0] - [24] > 4.5 in the *Spitzer* bands, i.e., colours that have been previously shown to select YSOs (see Jørgensen et al. 2007, for more details).

2.2. ^{13}CO Map

The ^{13}CO(1–0) data were obtained by the COMPLETE team[2] using the SEQUOIA focal plane array at the FCRAO telescope (Ridge et al. 2006). The region mapped covers ∼20 deg^2, with a 46″ angular resolution and 0.066 km s^{-1} velocity channels. The data were baseline-subtracted and sampled onto a 23″ grid; the average noise is 0.1 K (in T_A^* scale). Detailed comparisons between the molecular line data and extinction are presented in Pineda et al. (2008) and Goodman et al. (2009).

In our comparison of the N_2H^+, $C^{18}O$, and ^{13}CO spectra at the position of each core (Section 3), we fit a single Gaussian to each relevant ^{13}CO spectrum. The difference in N_2H^+ and ^{13}CO velocity centroids and ^{13}CO velocity dispersions are given in Table 1. All fits were visually examined; poor fits (i.e., where the spectra are not well-described by a single Gaussian) are also noted in Table 1. The estimation of the kinematic properties of

[1]A summary of all of the kinematic measures and their associated symbols used in this paper can be found in Table 5.

[2]All of the COordinated Molecular Probe Line Extinction Thermal Emission (COMPLETE) Survey data are publicly available at `http://www.cfa.harvard.edu/COMPLETE/`

the larger extinction regions using the ^{13}CO data are discussed in Section 4.

2.3. 2MASS Extinction

Extinction maps are now readily available for the entire sky (see Rowles & Froebrich 2009), allowing large-scale structures to be easily identified in all molecular clouds. A map of the extinction throughout the Perseus cloud has been produced based on reddening of stars in the 2MASS catalog (Ridge et al. 2006; KJD06). This map was created using the NICER technique (Lombardi & Alves 2001), and was presented in KJD06 and Ridge et al. (2006). The extinction map provides a useful dataset for defining the large-scale structures in Perseus. While this is not the only way to classify the large-scale column density structures, it has the advantage of being simpler than disentangling structures in a spectral cube. In datasets with clustered emission features, which are particularly prevalent in ^{13}CO maps of molecular clouds (and generally more common in 3D datasets), the emergent properties of the structures identified are particularly sensitive to the precise structure-identifying algorithm and parameters used (see, for example, Pineda et al. 2009). For our analysis here, we use the large-scale structures identified in KJD06 using the 2D version of the *clfind* (Williams, de Geus, & Blitz 1994) algorithm with a threshold of 3 mag and a stepsize of 1 mag on the extinction map smoothed to $5'$ resolution. The relevant properties of these extinction regions are summarized in KJD06 (Table 3) and KJT07 (Table 5). As a test, we also ran our analysis using the independently-defined large-scale regions in Pineda et al. (2008) based on CO centroid velocities and dust temperatures derived from IRAS data. Our conclusions are unchanged using these alternate regions, suggesting that our results are not strongly dependent on the definition of the regions used. We prefer to define the regions based on extinction, however, as this definition should be easy to apply to other observations and simulations.

Figure 1 summarizes the data analyzed in this paper. The greyscale image shows the integrated intensity of the ^{13}CO data, while the red circles show the N_2H^+ pointings. The total column density, as measured by the extinction observed in the 2MASS dataset is overlaid as black contours and the extinction regions are shown as coloured contours.

3. RELATIVE MOTIONS AT THE DENSE CORE POSITIONS

KJT07 measured the difference in centroid velocity of N_2H^+ and $C^{18}O$ ($v_{N2H+} - v_{C18O}$), reflecting the motion between the dense cores (N_2H^+) and their surrounding envelopes ($C^{18}O$)

along the line of sight. This relative motion was found to be smaller than the envelope velocity dispersion (σ_{C18O}) and for 90% of the cores, less than the sound speed, assuming a temperature of 15 K[3]. The small difference in centroid velocities implies that the dense core is dynamically coupled to its surrounding envelope, and appears to argue against the competitive accretion scenario (KJT07; Walsh et al 2004, but see also Ayliffe et al 2007). Since ^{13}CO(1–0) is sensitive to lower density material than C^{18}O(2–1), we can additionally compare the N_2H^+ and C^{18}O centroid velocities to that of the ^{13}CO to determine whether the tight correlation in velocities extends to the less dense material. (Note that the beamsize of the ^{13}CO observations is several times larger than that of the other tracers, so a larger physical volume of material is being traced, both in extent across the plane of the sky and along the LOS.)

Figure 2 shows the distribution of centroid velocity differences as a function of RA (left panel) and the overall distribution of values (right panel). The filled symbols (left) and solid lines (right) denote locations where the ^{13}CO Gaussian fits were deemed 'good' (roughly 87%), while the empty symbols and dotted lines denote locations where only the N_2H^+ and C^{18}O fits were good. Note that the ^{13}CO map did not extend to L1455, hence no 'good' fits in that region were possible. All of these data are also provided in Table 1. The greyscale image in the figure background shows the position-velocity (PV) diagram for the ^{13}CO gas, with the contours indicating the FWHM values. As can be seen from the figure, the spread in velocity difference is much smaller between N_2H^+ and C^{18}O than between N_2H^+ and ^{13}CO, and both of these are smaller than the range spanned by ^{13}CO emission at that RA. The standard deviation of the centroid velocity differences are 0.18 km s^{-1} for $v_{N2H+} - v_{C18O}$ at all locations, 0.19 km s^{-1} for $v_{N2H+} - v_{C18O}$ where good ^{13}CO fits exist, and 0.33 km s^{-1} for $v_{N2H+} - v_{13CO}$, while the errors in the centroid velocity differences measured are roughly 0.015 km s^{-1} for N_2H^+ and either CO species. A two-sided KS test[4] shows that the likelihood that both distributions are drawn from the same parent sample is only 2%. The sound speed is 0.23 km s^{-1} for the mean gas, assuming a temperature of 15 K and a mean molecular weight of $\mu = 2.33$. The largest velocity differences are found in the NGC 1333 region.

A second way to measure the relative motion between the species is to compare the difference in velocity to the velocity dispersion of the less dense species. This normalized

[3]In terms of the full three-dimensional picture, the full (3D) velocity difference between the core and envelope would be expected to be larger than we observe, since only the LOS components of the velocities are measurable. Similarly, the envelope velocity dispersion and sound speed discussed also only reflect LOS components of the full 3D motion; all are equally affected by projection.

[4]A two-sided KS test allows one to measure the probability of two distributions being drawn from the same parent distribution, (e.g., Lupton 1983).

velocity difference is written as:

$$\varsigma_{norm} = \frac{v_{N2H+} - v_{CO}}{\sigma_{CO}} \quad (1)$$

This quantity indicates whether the dense core moves within the typical range of motions present in the lower density environment, in this case, characterized by the gas along the same line of sight as the core. KJB09 showed that the normalized velocity difference can provide strong discrimination between numerical simulations with varying input levels of turbulence and magnetic field strengths. The normalized velocity difference was also one of the most discrepant measurements between many of the simulations analyzed in KJB09 and the observations of KJT07. Figure 3 shows the normalized velocity difference between the three species, as a function of RA (left panel) as well as the full distribution (right panel). As with the centroid velocity difference, we find the normalized velocity difference also tends to be quite small – nearly always less than one. The standard deviations of the normalized velocity differences are 0.20 (N_2H^+ - $C^{18}O$ at all positions), 0.22 (N_2H^+ - $C^{18}O$ where good ^{13}CO fits exist), and 0.39 (N_2H^+ - ^{13}CO), while the errors are 0.014 and 0.019 for N_2H^+ to $C^{18}O$ (all positions) and N_2H^+ to ^{13}CO respectively. A two-sided KS test shows that the likelihood that both distributions are drawn from the same parent sample is 0.2%. This indicates that the motions of the dense and less-dense gas are correlated (i.e., closer than expected from a random distribution), but less so at larger scales. This is perhaps not surprising, since the ^{13}CO observations trace not only a larger scale across the plane of the sky (due to the larger beamsize), but also are expected to trace a much larger scale along the LOS, and likely include emission from additional lower-density structures not associated with the dense core, due to ^{13}CO's sensitivity to lower density material than $C^{18}O$. Comparison with the results in Section 4.2 suggests that the agreement between N_2H^+ and ^{13}CO centroid velocities might become slightly stronger if the ^{13}CO beamsize was small enough to match the N_2H^+ beam. We expect, however, that the bulk of the difference is due to the larger scale of material traced by the ^{13}CO along the LOS, which would be unchanged with a smaller beamsize.

A slight skew is apparent in both N_2H^+ - ^{13}CO distributions, but does not appear to be physical. The mean velocity difference between N_2H^+ and ^{13}CO is 0.03 km s^{-1}, less than half the size of the ^{13}CO spectral resolution, and hence is likely due to stochastic effects. As a second check, we examined the velocity differences within each extinction region and found that there was no systematic offset; offsets of opposite directions were found in different regions.

4. DENSE CORES RELATIVE TO THE EXTINCTION REGIONS

4.1. Calculating Extinction Region Properties

Since a full map exists for the ^{13}CO data, it is also possible to quantify the motions of the dense cores within the larger extinction regions identified in KJD06. In order to more easily identify large-scale features in the regions, we first convolve and re-grid the ^{13}CO map to match the 2MASS extinction map angular resolution ($5'$) and grid. We create the mean ^{13}CO spectrum of the extinction region by summing all ^{13}CO spectra that lie within the contours of the extinction region boundaries of KJD06. We then calculate the centroid velocity, $v_{13CO,reg}$, and velocity dispersion, $\sigma_{reg,Gauss}$, of the spectrum using a single Gaussian fit. Note that these spectra are little affected by the prior map convolution to $5'$– in most cases, there is less than 3% variation between the Gaussian fit parameters for the total spectra of the convolved and un-convolved maps. Several of the spectra are not well-fit by a single Gaussian; in KJB09, we found that the full width of emission was better characterized by the full width at quarter maximum (FWQM). To determine the reliability of the Gaussian fits to the spectra, we also measure the FWQM for the ^{13}CO region spectra, following the procedure outlined in KJB09, and calculate $\sigma_{reg,FWQM}$, the sigma (1/e width) that would be measured if the spectrum were a perfect Gaussian with the measured FWQM. Table 2 provides the values fit to the cumulative spectra for each region using both methods, while Figure 4 shows both results for all of the regions. Three of the eleven extinction regions have significantly incomplete ^{13}CO coverage. Regions that are not well-covered may not provide a good representation of the overall region kinematics, regardless of the method used to fit the total spectrum. We set a minimum value of 80% coverage in the ^{13}CO observations for all of our subsequent analysis. Figure 4 shows that when a cutoff of 80% is applied, both measures of the total velocity dispersion ($\sigma_{reg,Gauss}$ or $\sigma_{reg,FWQM}$) produce similar results. For the remainder of the analysis and for the normalized velocity difference between the N_2H^+ cores and their associated extinction regions provided in Table 1, only the Gaussian fit results are used. Note that the tendency for the $\sigma_{reg,FWQM}$ measures to be slightly lower than the corresponding $\sigma_{reg,Gauss}$ value appears to be primarily caused by our limited resolution. While the FWQM is a good measure for identifying fainter, broad components of spectral lines, when significant line wings are not present, noise and the small number of spectral channels will tend to make the FWQM underestimate the true width, as this measure is not interpolated across spectral channels (unlike the Gaussian fit).

4.2. Analysis

Figure 5 shows the distribution of the centroid velocity differences between the N_2H^+ and the ^{13}CO region, $v_{N2H+} - v_{13CO,reg}$ versus RA (left panel), in addition to the full distribution of velocity differences (right panel). The motions between the core and region again tend to be small, although larger than the difference using the ^{13}CO velocity at the location of the dense core. The standard deviation of the distribution is 0.48 km s^{-1} (c.f. 0.33 km s^{-1} for ^{13}CO gas at the dense core location); the error in the velocity difference measured is roughly 0.011 km s^{-1}. Using a two-sided KS test shows that the probability of the distribution of velocity differences between the core and the ^{13}CO gas at the core's location versus over the entire region is only 0.5%. Figure 6 shows the distribution of normalized velocity difference between the cores and regions, $\zeta_{norm,reg}$ (calculated using eqn 1), versus RA (left panel) as well at the total distribution (right panel). The standard deviation of $\zeta_{norm,reg}$ is 0.5 (c.f. 0.39 for ^{13}CO gas at the dense core location) ; the error in the normalized velocity difference measured is 0.013. The two-sided KS test gives a probability that this normalized velocity difference and the one measured for the ^{13}CO at the core's location are drawn from the same parent distribution of 7%. We also examined the relationship between the velocity difference and the separation from the centre of the region, but found no discernable trend.

5. CORE KINEMATICS PER REGION

Most of the extinction regions contain multiple dense cores, thus the relationship between the ensemble of dense cores and the extinction region can also be examined. In particular, the core-to-core (v_{LSR}) motions can be compared to the spread of motions seen over the region as a whole in an "environmental" tracer (e.g., ^{13}CO); this should reveal how connected the dense cores are to the lower density gas in the region. If the dense cores are connected to the large-scale non-thermal motions, then the dispersion in the core centroid velocities would be expected to be similar to the global velocity dispersion of the region, as measured in ^{13}CO. If, however, the core-to-core motions are much smaller than the global velocity dispersion of the region, then this may be an indication that the dense cores have become detached from the large-scale motions within the cloud, arising from turbulent flows, for example. Alternatively, the spatial distribution of cores may lead to them tracing a smaller volume of material than the ^{13}CO.

5.1. Method of Calculation

Section 4.1 describes the calculation of the extinction region velocity dispersions. There are several approaches that can be taken to quantify the core-to-core motions within each extinction region. The first, method A, is a purely statistical measure, which involves simply taking the standard deviation of the centroid velocities of all of the dense cores within each region, $\sigma v_{meth.A}$. This is effective when the spectrum of each core is well described by a single, relatively narrow, velocity component. In cases where these conditions do not hold, interpretation of the standard deviation can be more difficult. This method also does not account for individual core linewidths, which could represent a significant fraction of the total dense gas velocity dispersion of the core gas. The second method, method B, accounts for both the core-to-core motion and the internal velocity dispersion through summing all of the spectra and measuring the resultant total velocity dispersion, $\sigma v_{meth.B}$. This method may be biassed if some cores are much brighter than others, and can be particularly challenging for molecules with hyperfine transitions, due to different components blending together in the summed spectrum. In KJT07, we adopted method A for measuring the N_2H^+ relative motions and method B for measuring the $C^{18}O$ relative motions; here, we again adopt method A for N_2H^+, but show that method B yields similar results. Note that any velocity gradient across the region is implicitly included in both measures and is not accounted for separately; the same is true for the extinction region veloctiy dispersion.

5.2. Results

Figures 7 through 12 qualitatively show our main result (examined in more detail below) – the dense cores have a much lower core-to-core velocity dispersion than the velocity dispersion of the ^{13}CO regions they reside in. In the top panel of each figure, a comparison is shown between the cumulative ^{13}CO spectrum across the entire region with measures of the dispersion seen in all the N_2H^+ dense cores. The dashed light green line shows the result for N_2H^+ from method A above (the standard deviation of the N_2H^+ centroid velocities, centered on the mean centroid velocity), while the dark green line shows the result from method B above (the dispersion of the sum of the N_2H^+ spectra). As well, the dark blue line shows the result from method B applied to the $C^{18}O$ spectra in the region. All of these cumulative spectra are compared to the region as a whole in ^{13}CO (black and grey shading). The figures show that the core-to-core velocity dispersion is similar when measured using either method A or method B, and that this velocity dispersion is significantly smaller than the velocity dispersion of the region as a whole.

We now determine the above result more rigorously. In KJT07, we preferred the use

of method A to measure the N_2H^+ core-to-core velocity dispersion, due to the difficulties associated with method B for N_2H^+ outlined in Section 5.1. In that work, only starless cores were considered, due to the potential for protostars to have inherited more motion from surrounding sources. Here, we measure the standard deviation both for the starless cores only as well as the full sample of cores (the full sample was plotted in Figures 7 to 12). Table 3 provides the values derived for the core-to-core velocity dispersion for both method A (both starless cores and the full sample) and for method B (full sample only). Figure 13 shows a comparison of the core-to-core velocity dispersion measured by method A for the starless cores ($\sigma v_{meth.A,sl}$) and all cores ($\sigma v_{meth.A,all}$) versus the velocity dispersion of the region ($\sigma_{13CO,reg}$). As can be seen in the figure, the core-to-core velocity dispersion tends to be similar in both samples; variations between the two may be attributed at least in part to small number statistics. The magnitude of variation expected due to small number sampling is further discussed in the following subsection.

The standard deviation of core centroid velocities measured in each extinction region is a good description of the width of the distribution, despite the small number of cores typically present. In the regions with a sufficient number of cores, we tested this in two ways. First, we ran KS tests and found that the distribution of velocities in each region was consistent with being drawn from a normal distribution with a median and standard deviation equal to the value measured, with over 80% probability in most cases. As a second test, we compared the standard deviation to the median absolute deviation, a robust measure of the width of distributions, i.e., little-effected by outlying points (e.g., Andersen 2008). For a normal distribution, the median absolute deviation is 1.48 times smaller than the standard deviation; using this conversion factor, we find the standard deviation as inferred from the median absolute deviation agrees to within 12%. Based on these tests, it is reasonable to assume that the standard deviation is a good descriptor of the width of the core centroid velocity dispersion within each region.

As Figure 13 suggests, there is no apparent variation with the core-to-core velocity dispersion with the region velocity dispersion. In fact, all are consistent with being originating from the same parent distribution. Two-sided KS tests of each pair of regions yields probabilities of 65% in all but one case (and 12% in the remaining case) that the core velocities are drawn from the same sample[5].

[5]All regions were compared with region 7, since that region has the largest number of cores. The median core velocity in each region was subtracted from all the core velocities prior to comparison to account for the large-scale velocity gradient across Perseus.

5.2.1. Effect of Sampling a Small Number of Cores

The difference in size between the core-to-core and ^{13}CO regional velocity dispersion is sufficiently large that it cannot be attributed to the small number of cores within each region except for the regions with a very small number of cores. We ran a set of simulations to determine the size of the error induced by using a small number of cores to measure the underlying total velocity dispersion. Scaling the regional velocity dispersion to a value of one, we selected a sample of N_{cores} objects with velocities randomly drawn from a normal distribution (using IDL's *randomn* function), and calculated the standard deviation of the object-to-object velocity. We ran 10000 simulations for each value of N_{cores}. Figure 14 shows the results of this calculation. The squares indicate the mean scaled velocity dispersion determined for the 10000 simulations for every value of N_{cores}, while the vertical lines indicate the 68.2% confidence levels, corresponding to the 1 σ level in a normal distribution. Sampling a very small number of cores tends to increase the difference between the measured and intrinsic velocity dispersion, but does not systematically lower the measured velocity dispersion by a significant amount when more than a few cores are present, in agreement with the full analytic result from statistics (see, e.g., Kenney 1939); note that the full expression for the bias in the standard deviation is more complex than the oft-quoted $\sqrt{n/(n-1)}$[6] and is important to use for very low number samples.

The diamonds in Figure 14 show the observed core-to-core velocity dispersions (including both the starless cores and protostars), scaled by the ^{13}CO velocity dispersion of the region. This figure clearly shows that all of the observed core-to-core velocity dispersions lie well below the range of values expected for a population of objects sharing the same velocity dispersion as the parent ^{13}CO gas. Weighting the ratios between the core-to-core and region velocity dispersions after correction for the bias in the standard deviation gives a value of 0.5 ± 0.1, for either the full sample, or when restricted to the regions with good spectral coverage. This implies that if all regions have similar ratios of core-to-core versus regional velocity dispersions, a ratio of around one half is a reasonable estimate.

We conclude from this analysis that the dense cores tend to have a much smaller core-to-core motion than is present in the mean ^{13}CO gas, roughly half the value, and that this result is not due to small number statistics.

---

[6]The full correction factor is $\sqrt{\frac{2}{n-1}} \quad \frac{\Gamma(\frac{n}{2})}{\Gamma(\frac{n-1}{2})}$

5.2.2. Effect of Spatial Sampling

Since the dense cores tend to be preferentially found concentrated within a small portion of the extinction region, it is reasonable to ask whether the difference in size of the core-to-core and total region velocity dispersions is caused by spatial sampling rather than a physical difference between the two. For example, the dense cores could be at the centre of the potential well of the region and thus naturally be expected to have a smaller velocity dispersion than the mean gas spanning the entire potential well. Here, we show that the core-to-core velocity dispersions are intrinsically smaller than the typical ^{13}CO velocity dispersions, even accounting for the difference in area sampled on the plane of the sky.

The bottom panel of Figures 7 through 12 show the total ^{13}CO spectrum for each extinction region with differing areas considered. The black line and grey shading (identical to the one in the bottom panel) represents the sum of all ^{13}CO spectra within the region. The purple line shows the result that would be obtained if only the spectra within the area spanned by the cores were considered. In order to obtain this estimate, we summed only the spectra that lie within the minimal box (in RA and dec) containing all of the dense cores within the region. The resultant spectrum is similar to the total (black) spectrum, and certainly is not similar in width to the core-to-core result (green lines on the top panels).

We also considered an even more restrictive case – the red line in the bottom panel of Figures 7 through 12 shows the resultant spectrum if the ^{13}CO spectra *only at the locations of the dense cores* are used in the summation. This again shows marked similarity to the spectrum for the region as a whole, although with a lower signal to noise level. The ^{13}CO spectra for each region when restricted to the area spanned by or locations of the dense cores can be somewhat narrower than the ^{13}CO spectrum over the entire region, however, this difference is not sufficient to explain the smaller-still distribution of core-to-core velocity dispersions within each region. We measured the ratio in the width (Gaussian sigma) fit to the areally-restricted ^{13}CO spectra versus the spectra for the entire region, and find values of 88 $\pm$ 11% and 86 $\pm$ 16% for the spectra for the region spanned by cores and at only the core locations, respectively. Since the core-to-core velocity dispersion is approximately 50% of the total region velocity dispersion, the bulk of the difference cannot be explained by the clustered locations of dense cores.

5.3. Interpretation

Our analysis indicates that the core-to-core velocity dispersion is significantly smaller than the velocity dispersion of the lower density ^{13}CO gas in the larger extinction regions

in which the cores are found. Although this result is robust against the potential biasses that we have investigated, interpretation is hampered by a lack of knowledge of the full 3D structure of the cloud. If, for example, the ^{13}CO within each extinction region can be thought of as belonging to a single, large, coherent entity, then the fact that the core-to-core velocity dispersions are significantly smaller than that of the entire region would indicate that the dense cores are more bound than the region as a whole. On the other hand, if the ^{13}CO gas actually comprises a number of smaller, independent structures along and across the LOS, then the ^{13}CO may have a larger velocity dispersion than the cores because of the multiple structures probed along the LOS. Even if the ^{13}CO gas comprises a single entity along the line of sight, if the dense cores probe only a fraction of this material, a smaller velocity dispersion would be expected. Larson's linewidth-size relationship (Larson 1981), for example, would predict a velocity dispersion half as large for the cores as the region if the cores traced a length scale roughly one quarter the length traced by ^{13}CO. We do not have any way to determine the three dimensional cloud structure, hence the ratio in core-to-core vs region velocity dispersion we measure cannot have a a definitive interpretation. It is, however, a straightforward benchmark that can be used to evaluate star formation models.

6. REGIONAL VELOCITY GRADIENTS

Finally, we analyze the large-scale features in the velocity structure of each extinction region. We calculate the gradient of ^{13}CO centroid velocities across each extinction region using the $5'$ convolved ^{13}CO data (see Section 4.1) and applying the gradient calculation method formulated in Goodman et al. (1993). Figures 15 and 16 show the centroid velocity measured for each cell in the convolved ^{13}CO map (colourscale) and the gradient measured (white arrows). The overall regional velocity gradient is shown in the bottom left corner of each plot. Table 4 provides the magnitude and orientation of the gradient measured in each region, along with the formal error to the gradients fit; note that these errors are often small due to the large number of points fit.

6.1. Cores Relative to the Gradient

If the dense cores are connected to the large-scale motions within each region, then they would be expected to follow the same large-scale gradient as is observed in ^{13}CO. We determine the velocity expected at each position in the region by using the velocity at the centre of the extinction region as a zero-point and extrapolating outwards using the gradient

measured, i.e.,

$$v_{flow,mod}(x,y) \quad = \quad v_{13CO}(x_c,y_c) + \mathcal{G}\cdot\mathbf{d} \tag{2}$$

or

$$v_{flow,mod}(x,y) \quad = \quad v_{13CO}(x_c,y_c) + \mid \mathcal{G} \mid d_{\parallel} \tag{3}$$

where v_{13CO} is the velocity observed at the central position (x_c, y_c), $\mathcal{G}$ is the gradient (in km s^{-1} pc^{-1}), d is the distance from (x, y) to (x_c, y_c), and $d_{\parallel}$ is the distance from (x, y) to (x_c, y_c) in the direction parallel to the gradient's direction.

Figure 17 shows the difference in core centroid velocity, v_{N2H+}, and the velocity inferred at the core's position from the regional velocity gradient, $v_{flow,mod}$ as a function of RA. As in Figure 2, the background greyscale image shows the PV diagram for ^{13}CO, with the value at each RA shifted so the peak intensity is at zero. A similar scatter in the velocity difference is found in all extinction regions.

The left panel of Figure 17 shows the distribution in velocity difference between the cores and the regional flow, $v_{N2H+} - v_{flow,mod}$ for the entire cloud (red), as well as the velocity difference between individual ^{13}CO pointings and the regional flow, $v_{13CO} - v_{flow,mod}$ (black). While the cores do not perfectly follow the gradient-determined velocity, they tend to have a deviation similar to that of the typical ^{13}CO gas; the standard deviations of both $v_{N2H+} - v_{flow,mod}$ and $v_{13CO} - v_{flow,mod}$ are 0.45 km s^{-1}.

6.2. Large-scale Energetics

The magnitude of the gradient across the region can be compared to the total velocity dispersion measured for the region. Regions dominated by large-scale motions such as shear or rotation, would be expected to have a high ratio of the velocity dispersion inferred from the gradient to the total velocity dispersion, whereas regions dominated by small-scale random motions would be expected to have a lower ratio.

We approximate the velocity dispersion inferred from the gradient across each region as the gradient multiplied by the diameter of the region. Since the ^{13}CO emission across each region is, to first order, constant, this is a (somewhat) better estimate than using, for example, the radius of the region; all locations along the region contribute approximately equally to the total region spectrum. (Note that this estimate would not be appropriate for centrally concentrated objects.) Figure 18 shows a comparison of the velocity dispersion inferred from the gradient across each region versus the total dispersion observed in ^{13}CO. The ratio of large-scale versus total velocity dispersion is around 50% for the regions with

well-determined measurements. A few of the regions show ratios above 100%, which can be understood by the fact that our estimate of the large-scale velocity dispersion is crude. For example, a varying column density across a region would tend to weight a limited range in velocities, and hence decrease the total velocity dispersion measured, while leaving the large-scale velocity dispersion determined from the gradient unchanged.

Turbulent motions that are dominated by large-scale modes can also produce an observable gradient. Burkert & Bodenheimer (2000, hereafter BB00) investigated the magnitude of the gradient expected from large-scale turbulent modes for cores similar to the NH_3 cores observed in Goodman et al. (1993, hereafter G93), Barranco & Goodman (1998, hereafter BG98), and Goodman et al. (1998). BB00 ran several thousand realizations of a 3D turbulent velocity field with power spectra of $P(k) \propto k^{-4}$ and $P(k) \propto k^{-3}$, where $P(k)$ is the power at wavenumber k; the oft-adopted Kolmogorov (incompressible turbulence) power spectrum falls within this range with $P(k) \propto k^{-11/3}$. Along with this turbulent velocity field, BB00 adopted a spherically symmetric, centrally-condensed density distribution. They then calculated the resultant spectra observable in 2D, and determined the gradient across the core using the same method as described in G93 (and also used in our analysis). The $P(k) \propto k^{-4}$ turbulent power spectrum has more power in the largest modes, and, as expected, was shown to generally produce larger observed gradients.

Although the BB00 models were run under the assumption of a single size scale (cores with a radius of 0.1 pc), BB00 assume a Larson-type scaling law with $\sigma \propto R^{0.5}$ to compare their results to that of the entire G93 sample of NH_3 cores. Figure 19 shows the velocity dispersions and diameters of the extinction regions we measure as well as the G93 NH_3 cores. The extinction regions follow a similar trend to the G93 cores, hence the BB00 models can be compared to the extinction regions in the same manner as was done for the G93 cores. In Figure 20, we show the BB00 predictions for gradients resulting from turbulent power spectra with $P(k) \propto k^{-4}$ and $P(k) \propto k^{-3}$ (diagonal lines), as well as the G93 data (triangles) and our own ^{13}CO measurements (diamonds). For comparison, we also show a recent measurement of the size and velocity gradient of an embedded protostar (IRS 1) within the isolated Bok globule, BHR 71 (Chen et al. 2008). To plot the G93 data, we adopt the same procedure as BB00 – the diameter used is the geometric mean of the G93 FWHM sizes of the major and minor axes, and updated gradient measurements for the seven sources in BG98 replace those from G93. The solid diagonal lines indicate the most likely values of the gradient found in the BB00 simulations, while the dotted lines indicate the half maximum likelihood values. While the extinction regions we analyze are larger than the cores in G93, our observations clearly follow the same trend predicted by the BB00 model. Although the centrally concentrated density distribution adopted in the BB00 model is not a good representation of the density distribution in the regions we analyze, BB00 state that their

results are not strongly dependent on the density distribution – they found similar results when a constant density distribution was adopted. The extension of their predictions to the ^{13}CO gradients in the extinction regions measured here is therefore reasonable. A generalized formulation of the velocity gradient for various density profiles and turbulent power spectra is given in Kratter & Matzner (2006), and also shows similar results are expected regardless of the assumed density distribution.

7. DISCUSSION – ENERGETICS

The above analyses all point towards a common picture of the energetics of dense cores within the context of the molecular clouds they inhabit. Previous work (e.g., KJT07) has shown that dense cores have little motion with respect to their immediate surrounding gas. Our analysis comparing the N_2H^+ and ^{13}CO data has shown that the small motions continue to larger scales. Within the larger extinction regions that the cores inhabit, the cores have smaller core-to-core velocity dispersions than the typical ^{13}CO gas. Interpretation of this observation is hampered by the lack of knowledge of the full 3D structure of the lower density cloud material. The lower density gas traced by ^{13}CO may be tracing multiple structures (or a larger length scale) along the line of sight that the cores are not associated with.

The large-scale low density gas appears to be dominated by turbulent motions. Across each extinction region, the gradients in ^{13}CO centroid velocity were measured and appear to account for roughly half of the total velocity dispersion of the region. This is approximately the same size as is predicted to arise from large-scale modes of a turbulent power spectrum with $P(k) \propto k^{-4}$ (BB00). The velocities of the dense cores within each extinction region follow the velocity gradient found in the ^{13}CO gas. This is consistent with a picture where both the dense cores and ^{13}CO gas obey Larson's Laws; the cores trace a smaller volume of gas than the ^{13}CO both across the plane of the sky and along the line of sight, and so show a smaller core-to-core velocity dispersion than the regional ^{13}CO velocity dispersion, while still tracing the same large-scale velocity gradient. A direct comparison of the ratio in the core-to-core and extinction region velocity dispersions with the prediction from Larson's Laws could be made once similar measurements exist for several molecular clouds. Determining this effect quantitatively for a single region is complicated by the lack of knowledge of the line of sight distribution of cores and ^{13}CO. With a large enough sample of regions, however, this effect should be quantifiable across the ensemble.

Comparison of the data to expectations from virial equilibrium is unclear at best. As usual, the surface terms of the virial equation are unknown and must be excluded. In addition, the gas within each extinction region must be assumed to be a single coherent

entity both across the sky and along the line of sight and the substantial velocity gradient across each region discussed above must also be ignored. With these many assumptions, the virial velocity dispersion of each region could then be estimated in some of the traditional ways – using the mass and size of each region (as in KTJ07) or using the ^{13}CO velocity dispersion as a proxy (similar to Larson 1981). The core-to-core motion within each region would then be interpreted as "sub-virial", since their velocity dispersion is much smaller than either of these two estimates of the region's virial velocity dispersion. Given the questionable assumptions that are required to make the virial argument, in particular ignoring the large-scale gradient across each region and the possibility of multiple structures along the line of sight, we do not recommend interpreting the data under this framework. Instead, future 'observations' of numerical simulations will be able to reveal the range of physical conditions that can match our results.

8. CONCLUSIONS

We analyze the kinematic relationship between dense cores and the larger environments they inhabit using pointed N_2H^+ and $C^{18}O$ observations (KJT07) as well as a ^{13}CO spectral cube (Ridge et al. 2006; Pineda et al. 2008) of the Perseus molecular cloud. We present a series of kinematic measures complementing those in (KJT07) that can be used to test models of star formation. We choose to investigate physically-motivated, but procedurally straightforward measures of kinematics in Perseus. Through this, we hope that future simulations and as well as observations of other star-forming regions will adopt similar measures to allow constraints of models of star formation across differing environments.

We find the dense cores have small motions with respect to the ^{13}CO gas along the same line of sight, with a standard deviation of 0.33 km s^{-1}, or 0.39 times the ^{13}CO velocity dispersion at that location, while the sound speed in the ambient medium is ~ 0.23 km s^{-1}. The small motions we measure are an upper limit on the true motion between the N_2H^+ and ^{13}CO, since the ^{13}CO data have a beamsize roughly twice the size of the N_2H^+ data. The ^{13}CO may also be tracing additional kinematic structures that are not traced by N_2H^+. The core-to-core motions within the larger extinction regions they inhabit are about half of the total (^{13}CO) velocity dispersion within the region. The dense cores tend to follow the overall velocity gradient across each extinction region to the same extent as the ^{13}CO gas. The gradients across each extinction region tend to account for roughly half of the total measured velocity dispersion, and are of the magnitude as expected by large-scale turbulent modes following a power spectrum of $P(k) \propto k^{-4}$ (Burkert & Bodenheimer 2000). The kinematic measures presented here should be relatively straighforward to obtain both

in other large observational datasets as well as numerical simulations of star formation. Together with the measures presented in KJT07, we provide a set of benchmarks by which future star formation models can be evaluated.

We would like to thank Stella Offner for partipating in a series of lively discussions amongst the authors on various projection effects and for providing a quick analysis of a core in a 3D simulation in order to test several ideas. HK also thanks Fabian Heitsch for an informative discussion on velocity gradients caused by large-scale modes of turbulence. Finally, we would like to thank the referee for a thorough and thoughtful report which improved our paper, particularly in the statistics presented.

HK is supported by a Natural Sciences and Engineering Research Council of Canada Postdoctoral Fellowship, with additional support from the SAO. DJ is supported by a Natural Sciences and Engineering Research Council of Canada grant. JEP is supported by the NSF through grant #AF002 from the Association of Universities for Research in Astronomy, Inc., under NSF cooperative agreement AST-9613615 and by Fundación Andes under project No. C-13442. Support for this work was provided by the NSF through awards GSSP06-0015 and GSSP08-0031 from the NRAO. This material is based upon work supported by the National Science Foundation under Grant No. AST-0407172 and AST-0908159 to AAG.

A. GLOSSARY OF KINEMATIC MEASURES

A large number of kinematic measures are presented in this paper in order to provide a variety of diagnostics on the molecular cloud. For clarity, Table 5 summarizes all of these kinematic measures, along with a brief description of their meaning.

REFERENCES

Andersen, R. 2008, Modern Methods for Robust Regression, Issue 152, pp 16, SAGE Publications

André, P. & Saraceno, P. 2005, ESASP, 577, 179

Arce, H. G., Borkin, M. A., Goodman, A. A., Pineda, J. E., & Halle, M. W. 2010, ApJ accepted

Ayliffe, B. A., Langdon, J. C., Cohl, H. S., & Bate, M.R. 2007, MNRAS, 374, 1198

Barranco, J. A., & Goodman, A. A. 1998, ApJ, 504, 207

Burkert, A. & Bodenheimer, P. 2000, ApJ, 543, 822

Černis, K. 1993, BaltA, 2, 214

Chen, X., Laundhardt, R., Bourke, T. L., Henning, T., & Barnes, P. J. 2008, ApJ, 683, 862

Enoch, M. L. et al. 2006, ApJ, 293

Evans, N. J. et al. 2003, PASP, 115, 965

Goodman, A. A., Benson, P. J., Fuller, G. A. & Myers, P. C. 1993, ApJ, 406, 528

Goodman, A. A., Barranco, J. A., Wilner, D. J., & Heyer, M. H. 1998, ApJ, 504, 223

Goodman, A. A., Pineda, J. E., & Schnee, S. L. 2009, ApJ, 692, 91

Hatchell, J., Richer, J. S., Fuller, G. A., Qualtrough, C. J., Ladd, E. F., & Chandler, C. J. 2005, A&A, 440, 151

Hatchell, J., Fuller, G. A., Richer, J. S., Harries, T. J., & Ladd, E. F. 2007, A&A, 468, 1009

Hatchell, J., Fuller, G. A., & Richer, J. S. 2007, A&A, 472, 187

Johnstone, D., Rosolowsky, E., Tafalla, M., & Kirk, H. 2010, ApJ, 711, 655

Jørgensen, J. K., Johstone, D., Kirk, H., & Myers, P. C. 2007, ApJ, 656, 293

Kenney, J. F. 1939, The Mathematics of Statistics, Part II, pp 135 (7.7) and 127 (7.3), D van Nostrand Co Inc, NY

Kirk, H., Johnstone, D., & Di Francesco, J. 2006, ApJ, 646, 1009

Kirk, H., Johnstone, D., & Tafalla, M. 2007, ApJ, 668, 1042

Kirk, H., Johnstone, D., & Basu, S. ApJ, 699, 1433

Klessen, R. S., Ballesteros-Paredes, J., Vázquez-Semadeni, E., Duran-Rojás, C. 2005, ApJ, 620, 786

Kratter, K. M. & Matzner, C. D. 2006, MNRAS, 373, 1563

Larson, R. B. 1981, MNRAS, 194, 809

Lombardi, M. & Alves, J. 2001, A&A, 377, 1023

Lupton, R. 1983, Statistics in Theory and Practice, Princeton University Press, New Jersey, USA

McKee, C. F. 1989, ApJ, 345, 782

Offner, S. S. R., Klein, R. I., & McKee, C. F. 2008, ApJ, 136, 404

Pineda, J. E., Caselli, P., & Goodman, A. A. 2008, ApJ, 679, 481

Pineda, J. E., Rosolowsky, E. W., Goodman, A. A. 2009, ApJ, 699L, 134

Rebull, L. M. et al. 2007, ApJS, 171, 447

Ridge, N. A., Di Francesco, J., Kirk, H., Li, D., Goodman, A. A., et al. 2006, AJ, 131, 2921

Rosolowsky, E. W., Pineda, J. E., Foster, J. B., Borkin, M. A., Kauffmann, J., Caselli, P., Myers, P. C., Goodman, A. A. 2008, ApJS, 175, 509

Rowles, J. & Froebrich, D. 2009, MNRAS, 395, 1640

Tafalla, M., Myers, P. C., Caselli, P., Walmsley, C. M., Comito, C. 2002, ApJ, 569, 815

Walawender, J., Bally, J., Reipurth, B., & Aspin, C. 2004, AJ, 127, 2809

Walsh, A. J., Myers, P. C. & Burton, M. G. 2004, ApJ, 614, 194

Ward-Thompson, D. et al. 2007, PASP, 119, 855

Williams, J.P., de Geus, E.J., & Blitz, L. 1994, ApJ, 428, 693

Table 1. N_2H^+ to CO Relative Motions

	$C^{18}O$ [a]		^{13}CO point [b]				^{13}CO region [d]		
N_2H^+ [a] #	$v_{N2H+} - v_{C18O}$ (km s^{-1})	σ_{C18O} (km s^{-1})	$v_{N2H+} - v_{13CO}$ (km s^{-1})	σ_{13CO} (km s^{-1})	Good Fit?	Region[c] #	$v_{N2H+} - v_{13CO,reg}$ (km s^{-1})	$\sigma_{13CO,reg}$ (km s^{-1})	Good Fit?
4	0.13	0.91	0.11	0.58	Y	1	0.19	0.64	Y
5	0.01	1.00	0.21	0.64	Y	1	0.15	0.64	Y
6	0.19	0.86	0.35	0.67	Y	1	0.32	0.64	Y
8	-0.13	0.53	-0.19	0.50	Y	1	0.02	0.64	Y
12	-0.10	0.40	0.32	0.69	Y	1	0.71	0.64	Y
13	0.01	0.41	0.44	0.67	Y	1	0.94	0.64	Y
15	-0.17	0.86	-0.09	0.61	Y	2	0.14	0.91	Y
16	0.06	1.36	0.50	0.78	Y	2	1.07	0.91	Y
18	0.33	1.23	0.54	0.83	Y	2	1.12	0.91	Y
19	-0.01	0.67	0.03	0.64	Y	2	-0.25	0.91	Y
20	0.02	0.62	0.14	0.65	Y	2	-0.23	0.91	Y
21	0.20	1.00	0.41	0.71	Y	2	0.22	0.91	Y
22	-0.49	1.13	-0.55	0.68	Y	2	-0.69	0.91	Y
23	0.02	0.75	-0.19	0.82	Y	2	-0.53	0.91	Y
24	-0.02	0.85	0.17	0.75	Y	2	-0.06	0.91	Y
25	0.12	0.81	0.32	0.64	Y	2	0.26	0.91	Y
26	0.04	0.57	-0.22	0.67	Y	2	-0.24	0.91	Y
27	-0.48	0.57	-0.54	0.55	Y	2	-0.56	0.91	Y
27	-0.02	0.57	-0.08	0.55	Y	2	-0.10	0.91	Y
28	-0.21	0.98	-0.42	0.57	Y	2	-0.34	0.91	Y
30	0.10	0.44	0.19	0.56	Y	2	0.04	0.91	Y
33	0.11	0.50	0.65	0.79	N	2	0.65	0.91	Y
34	-0.03	0.58	-0.20	0.63	Y	2	-0.59	0.91	Y
36	0.03	0.35	0.26	0.61	Y	2	0.59	0.91	Y
41	0.06	0.39	0.39	0.89	Y	2	-0.35	0.91	Y
53	0.10	0.50	0.36	0.65	Y	3	0.73	1.01	Y
55	0.06	0.50	0.57	0.90	N	3	0.45	1.01	Y
63	-0.06	0.64	-0.08	0.70	Y	4	-0.35	0.88	Y
67	-0.40	1.00	-0.66	0.71	Y	5	-0.46	0.89	Y
68	0.11	1.04	0.31	0.92	Y	5	0.23	0.89	Y
71	0.25	0.85	-0.07	0.85	Y	5	-0.03	0.89	Y
72	-0.20	1.20	-0.38	0.94	Y	5	-0.42	0.89	Y
73	-0.22	0.95	-0.24	0.81	Y	5	-0.26	0.89	Y
74	-0.09	0.86	-0.18	0.70	Y	5	0.15	0.89	Y
75	-0.07	0.89	-0.16	0.83	Y	5	-0.06	0.89	Y
76	-0.12	0.73	-0.20	0.61	Y	5	-0.18	0.89	Y
77	-0.04	0.79	-0.15	0.84	Y	5	-0.05	0.89	Y
78	-0.01	1.09	-0.19	0.91	Y	5	-0.02	0.89	Y
79	0.25	1.02	0.09	0.91	Y	5	0.13	0.89	Y
84	-0.21	0.79	0.23	0.96	Y	5	-0.08	0.89	Y
85	-0.09	0.98	-0.16	0.71	Y	5	-0.28	0.89	Y
86	0.01	0.96	0.25	0.74	Y	5	0.21	0.89	Y
87	0.00	0.41	-0.48	0.85	Y	5	-0.79	0.89	Y
90	-0.07	1.08	-0.19	0.94	Y	6	0.41	0.91	Y

Table 1—Continued

	$C^{18}O$ [a]		^{13}CO point [b]				^{13}CO region [d]		
N_2H^+ [a] #	$v_{N2H+} - v_{C18O}$ (km s^{-1})	σ_{C18O} (km s^{-1})	$v_{N2H+} - v_{13CO}$ (km s^{-1})	σ_{13CO} (km s^{-1})	Good Fit?	Region[c] #	$v_{N2H+} - v_{13CO,reg}$ (km s^{-1})	$\sigma_{13CO,reg}$ (km s^{-1})	Good Fit?
91	0.05	0.56	0.68	0.87	Y	–	–	–	N
92	0.02	0.57	–	–	–	6	-0.44	0.91	Y
93	-0.23	0.60	–	–	–	6	-0.58	0.91	Y
94	-0.08	0.67	–	–	–	6	-0.62	0.91	Y
95	0.05	0.52	-0.07	0.39	Y	7	0.53	1.25	Y
96	0.01	0.71	-0.10	1.17	N	7	-0.08	1.25	Y
97	-0.01	0.49	-0.00	0.48	Y	7	-0.12	1.25	Y
98	0.08	1.05	-0.29	0.91	Y	7	-0.15	1.25	Y
99	0.01	0.39	-0.09	0.74	N	7	-0.08	1.25	Y
99	0.00	0.46	-0.72	0.74	N	7	-0.71	1.25	Y
100	-0.03	0.71	-0.14	0.81	Y	7	-0.10	1.25	Y
101	-0.14	1.42	0.27	1.15	Y	7	0.59	1.25	Y
102	0.12	1.11	0.18	1.04	N	7	0.22	1.25	Y
103	0.19	0.86	-0.58	1.22	Y	7	-0.83	1.25	Y
103	0.55	0.86	-0.22	1.22	Y	7	-0.47	1.25	Y
104	0.05	1.41	0.88	1.57	Y	7	0.97	1.25	Y
106	0.19	1.92	0.06	1.19	Y	7	-0.13	1.25	Y
107	0.25	0.41	-0.38	1.22	Y	7	-0.38	1.25	Y
109	-0.04	1.49	0.62	1.51	Y	7	0.86	1.25	Y
110	0.41	1.88	0.43	1.26	Y	7	0.35	1.25	Y
111	0.14	1.59	-0.52	1.25	Y	7	-0.80	1.25	Y
111	0.35	2.13	0.40	1.25	Y	7	0.12	1.25	Y
112	0.22	1.51	0.65	1.38	Y	7	0.78	1.25	Y
113	0.24	1.46	0.36	1.18	Y	7	0.35	1.25	Y
115	-0.30	1.53	-0.20	1.22	Y	7	-0.46	1.25	Y
116	-0.17	1.53	0.04	1.01	Y	7	0.21	1.25	Y
118	-0.28	1.31	-0.27	1.21	Y	7	-0.28	1.25	Y
118	0.12	1.31	0.13	1.21	Y	7	0.12	1.25	Y
121	-0.06	0.92	0.20	0.94	Y	7	-0.40	1.25	Y
122	-0.08	0.96	-0.29	0.74	N	7	0.36	1.25	Y
123	-0.15	0.94	-0.18	0.72	N	7	0.57	1.25	Y
124	0.13	1.57	0.06	0.98	Y	7	-0.58	1.25	Y
125	-0.07	0.70	-0.46	0.93	Y	7	-0.34	1.25	Y
126	-0.02	1.64	-0.17	1.12	Y	7	-0.78	1.25	Y
127	0.04	0.43	-0.02	0.46	Y	9	0.18	0.87	Y
128	0.07	1.40	-0.28	1.13	N	7	-0.41	1.25	Y
129	0.01	0.23	–	–	–	9	-0.80	0.87	Y
130	-0.01	0.67	–	–	–	9	-0.51	0.87	Y
131	0.05	0.38	–	–	–	9	-0.58	0.87	Y
132	-0.37	1.01	–	–	–	9	-0.59	0.87	Y
133	-0.16	1.07	–	–	–	9	-0.30	0.87	Y
134	-0.04	0.70	–	–	–	9	-0.49	0.87	Y
135	0.04	0.70	–	–	–	9	-0.64	0.87	Y
136	0.24	1.34	–	–	–	9	-0.72	0.87	Y

Table 1—Continued

N_2H^+ [a] #	$C^{18}O$ [a] $v_{N2H+} - v_{C18O}$ (km s^{-1})	$C^{18}O$ [a] σ_{C18O} (km s^{-1})	^{13}CO point [b] $v_{N2H+} - v_{13CO}$ (km s^{-1})	^{13}CO point [b] σ_{13CO} (km s^{-1})	Good Fit?	Region[c] #	^{13}CO region [d] $v_{N2H+} - v_{13CO,reg}$ (km s^{-1})	^{13}CO region [d] $\sigma_{13CO,reg}$ (km s^{-1})	Good Fit?
136	0.04	0.45	–	–	–	9	0.58	0.87	Y
138	-0.17	0.90	–	–	–	9	-0.29	0.87	Y
139	0.17	0.97	–	–	–	9	-0.27	0.87	Y
140	0.00	0.27	–	–	–	9	-0.02	0.87	Y
143	0.00	0.46	0.12	0.56	Y	9	-0.27	0.87	Y
145	-0.18	1.31	-0.42	0.60	N	10	-0.94	0.81	Y
146	0.15	0.88	0.06	0.71	Y	10	0.13	0.81	Y
147	0.09	0.86	0.05	0.70	Y	10	0.28	0.81	Y
148	-0.25	0.53	0.35	0.80	Y	10	0.75	0.81	Y
148	0.22	1.02	0.27	0.80	Y	10	0.67	0.81	Y
149	0.16	1.07	0.01	0.79	N	10	0.15	0.81	Y
150	-0.04	0.68	-0.20	0.74	N	10	-0.31	0.81	Y
151	0.11	0.56	0.08	0.47	Y	11	0.23	0.88	Y
152	0.03	0.74	-0.04	0.62	N	10	-0.28	0.81	Y
155	0.04	0.49	-0.20	0.45	N	11	-0.14	0.88	Y

[a]N_2H^+ core number, N_2H^+ to $C^{18}O$ relative velocity, and $C^{18}O$ velocity dispersion from Kirk, Johnstone & Tafalla (2007).

[b]N_2H^+ to ^{13}CO relative velocity, ^{13}CO velocity dispersion at the point of the N_2H^+ observation, and whether the ^{13}CO fit was deemed good. Only good fits were used in the analysis.Dashes denote regions where ^{13}CO data does not exist.

[c]Associated extinction region.

[d]N_2H^+ to ^{13}CO relative velocity, ^{13}CO linewidth for the region and whether the ^{13}CO fit was deemed good. Only good fits were used in the analysis.

Table 2. Region Velocity Dispersions in ^{13}CO

Region [a] #	Areal [a] Cov. (%)	$\sigma_{reg,Gauss}$ [b] (km s^{-1})	Good [b] Fit?	$\sigma_{reg,FWQM}$ [c] (km s^{-1})
1	100	0.64	Y	0.60
2	100	0.91	Y	0.88
3	95	1.01	N	0.98
4	55	0.88	N	1.06
5	100	0.89	Y	0.86
6	52	0.91	Y	0.86
7	100	1.25	N	1.22
8	100	0.90	Y	0.84
9	40	0.87	Y	0.82
10	100	0.81	Y	0.74
11	84	0.88	Y	0.84

[a]Extinction region number and fractional coverage of the area observed in ^{13}CO over the extinction region.

[b]The Gaussian-fit ^{13}CO region velocity dispersion and whether the fit was judged to be good.

[c]The equivalent ^{13}CO region velocity dispersion as measured from the FWQM. See text for details.

Table 3. Core-to-Core Velocity Dispersions

Region #	$\sigma v_{sl,A}$ [a] (km s^{-1})	$\sigma v_{all,A}$ [a] (km s^{-1})	$\sigma v_{all,B}$ [b] (km s^{-1})
1	0.39	0.36	0.35
2	0.55	0.54	0.31
3	0.20	0.20	0.20
4	–	–	0.14
5	0.28	0.28	0.21
6	0.09	0.49	0.20
7	0.54	0.50	0.56
8	–	–	–
9	0.32	0.38	0.41
10	0.55	0.56	0.35
11	0.26	0.26	0.26

[a]Core-to-core velocity dispersion derived for starless cores and all cores using method A. Dashes denote regions with less than two cores. See text for details.

[b]Core-to-core velocity dispersion derived for all cores using method B. Dashes denote regions with no cores. See text for details.

Table 4. ^{13}CO Gradients Across Each Extinction Region

Region [a] #	$\mathcal{G}$ [b] (km s $^{-1}$ pc $^{-1}$)	Error [b] (km s $^{-1}$ pc $^{-1}$)	Angle [c] (degrees)	Error [c] (degrees)	D_{reg} [d] (pc)	$\mid \mathcal{G} \mid D_{reg}$ [e] (km s^{-1})
1	0.1456	0.0009	84.3	0.3	1.88	0.27
2	0.1115	0.0002	-118.78	0.08	2.71	0.30
3	0.1845	0.0007	84.5	0.2	1.79	0.33
4	0.811	0.002	-132.5	0.1	1.63	1.32
5	0.2252	0.0004	-82.98	0.07	1.40	0.32
6	0.667	0.005	23.4	0.3	1.10	0.73
7	0.3230	0.0003	-6.11	0.04	2.16	0.70
8	0.827	0.003	-48.6	0.1	1.10	0.91
9	0.934	0.005	-56.1	0.2	1.09	1.01
10	0.420	0.002	-42.3	0.2	0.94	0.39
11	0.627	0.002	-33.4	0.1	0.75	0.47

[a]The extinction region number

[b]The velocity gradient and associated error measured across each extinction region. See Section 6 for more detail.

[c]Orientation of the gradient and associated error. The angle is given in degrees clockwise from North.

[d]Extinction region diameter from KJD06.

[e]The velocity dispersion inferred from the gradient across each region.

Table 5. Summary of Kinematic Measures Used

Symbol	Formula	Description
v_x		Centroid velocity of species x
σ_x		Velocity dispersion (Gaussian sigma) of species x
	$v_{N2H+} - v_x$	Relative motion between N_2H^+ and species x
$\zeta_{norm,x}$	$\frac{v_{N2H+}-v_x}{\sigma_x}$	Normalized relative motion
$\sigma_{reg,Gauss}$		Region velocity dispersion using a Gaussian fit [a]
$\sigma_{reg,FWQM}$	$FWQM_{reg}/4ln\sqrt{2}$	Region velocity dispersion measured using the full width at quarter maximum [a]
$\sigma v_{meth.A}$	$\sigma(v)$	Dispersion of core centroid velocities within an extinction region ("method A")
$\sigma v_{meth.B}$		Velocity dispersion of the cores within an extinction region ("method B") [b]
D_{reg}		Diameter of extinction region
$\mathcal{G}$		Velocity gradient across a region
(x_c, y_c)		position of centre of region used in gradient calculation
$d_{\parallel}$		Distance between (x, y) and (x_c, y_c) parallel to the gradient
$v_{flow,mod}(x, y)$	$v(x_c, y_c)+ \mid \mathcal{G} \mid d_{\parallel}$	Velocity inferred from the bulk gradient
$\sigma_{reg,mod}$	$\mathcal{G} \times D_{reg}$	Region velocity dispersion inferred from the bulk gradient

[a]Measured using the cumulative spectrum of the entire extinction region

[b]Measured using the cumulative core spectra within the extinction region

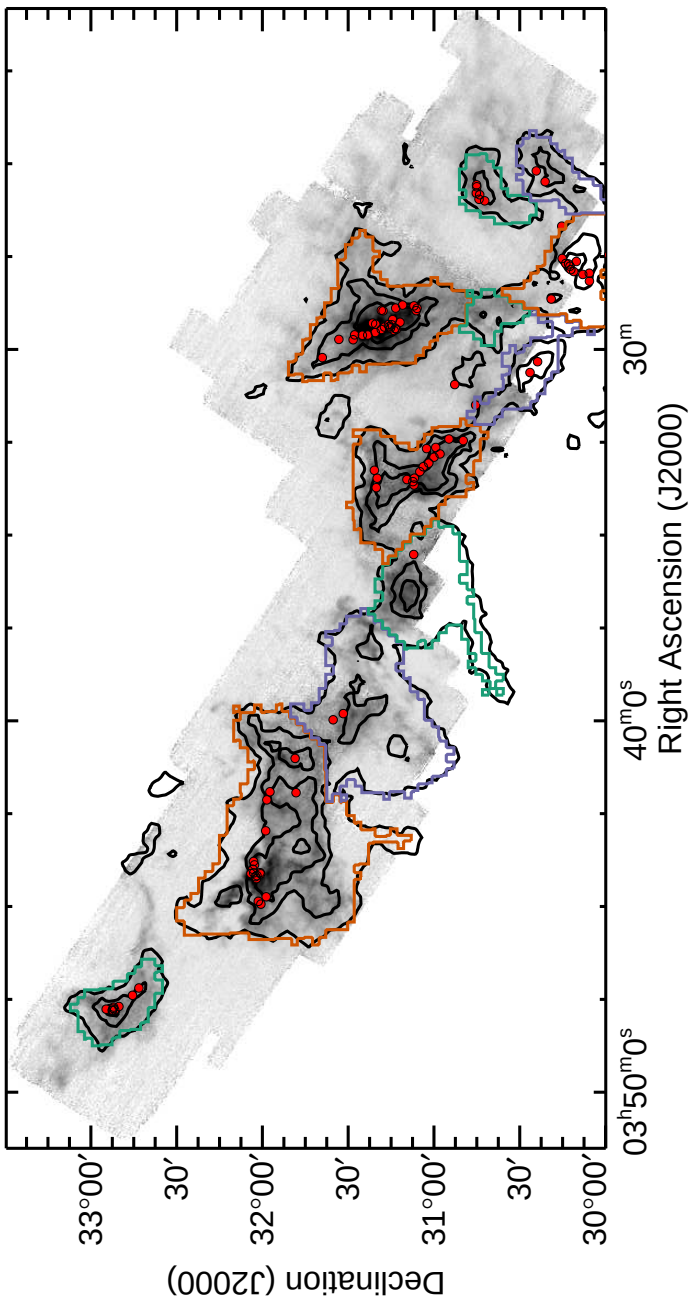

Fig. 1.— The greyscale image shows the ^{13}CO integrated intensity map from the FCRAO telescope. The overlaid black contours show extinction measurements derived from 2MASS data at levels of A_V = 3, 5, and 7 mag. The red circles show the locations of all of the IRAM 30 m N_2H^+ observations. The extinction regions used in the analysis here are denoted by the coloured contours. See text for details.

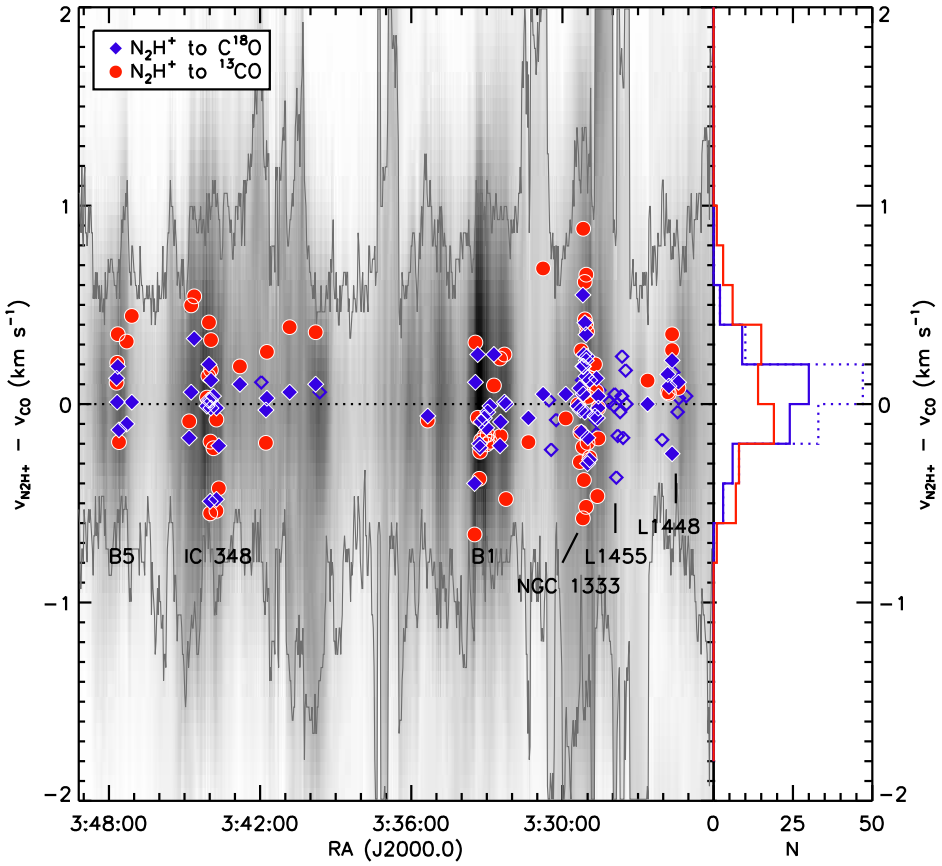

Fig. 2.— The distribution of centroid velocity difference between N_2H^+, $C^{18}O$, and ^{13}CO as a function of RA (left panel), and the full distribution (right panel). In the left panel, the blue diamonds indicate the distribution of $v_{N2H+} - v_{C18O}$, while the red circles indicate the distribution of $v_{N2H+} - v_{13CO}$. The empty diamonds indicate locations where there is no good Gaussian fit to the ^{13}CO data (or ^{13}CO observations do not exist), while the filled diamonds indicate where there is a good Gaussian fit to the ^{13}CO data. The greyscale image shows the position-velocity diagram for the ^{13}CO gas and the grey contours show the half-maximum value at every RA. At each RA, the cumulative spectrum has been shifed so that the peak intensity falls at a value of zero on the diagram. The greyscale ranges from 2 K km s^{-1} (black) to 0 K km s^{-1} (white). The approximate RA of well-known star forming regions are indicated by the text. In the right panel, the dotted blue line indicates the full distribution of $v_{N2H+} - v_{C18O}$, while the solid blue line shows only the points where there is a good Gaussian fit to the ^{13}CO data. The distribution of $v_{N2H+} - v_{13CO}$ is shown in red.

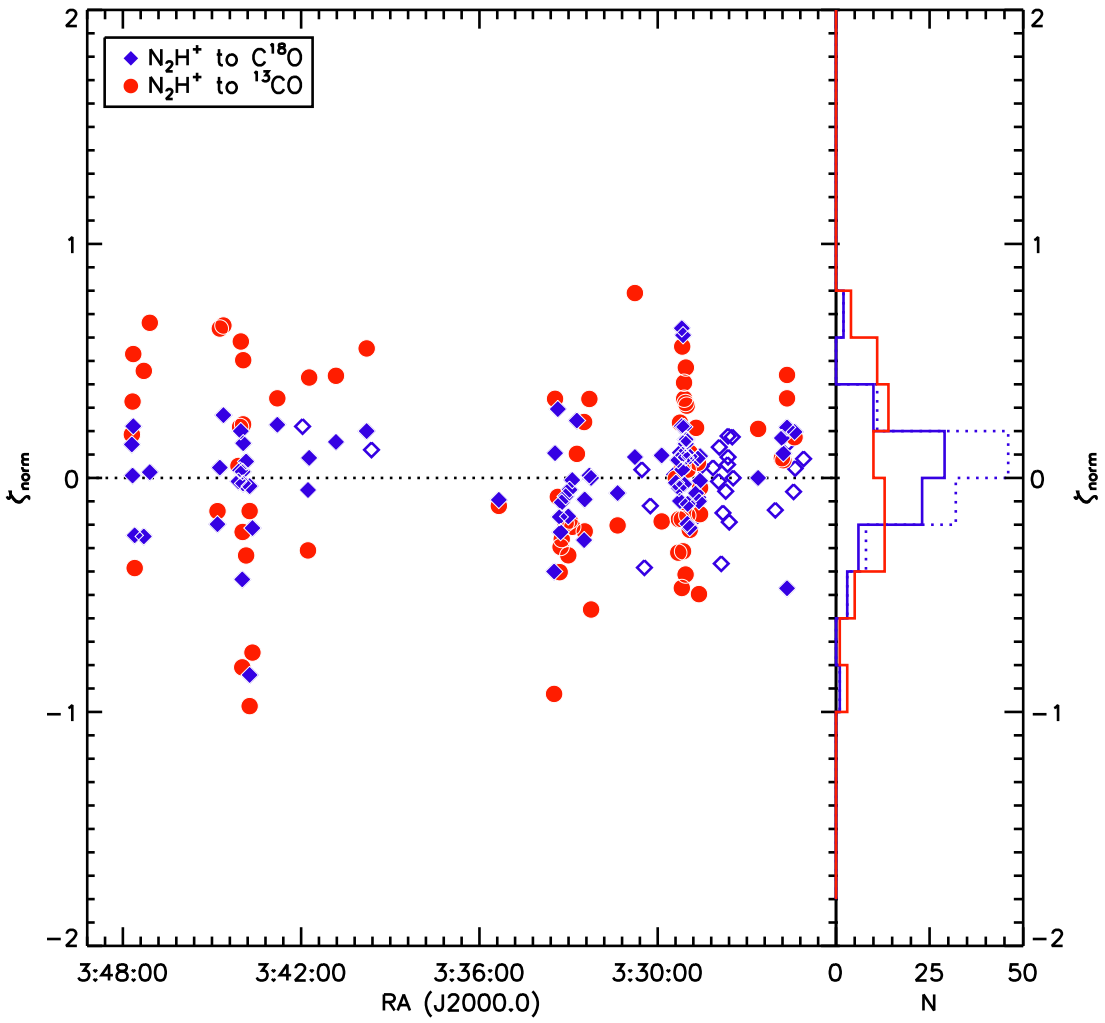

Fig. 3.— The distribution of normalized velocity differences, ζ_{norm}, between N_2H^+, $C^{18}O$, and ^{13}CO as a function of RA (left panel). The total distribution is shown in the right panel. See Figure 2 for details on the plotting conventions used.

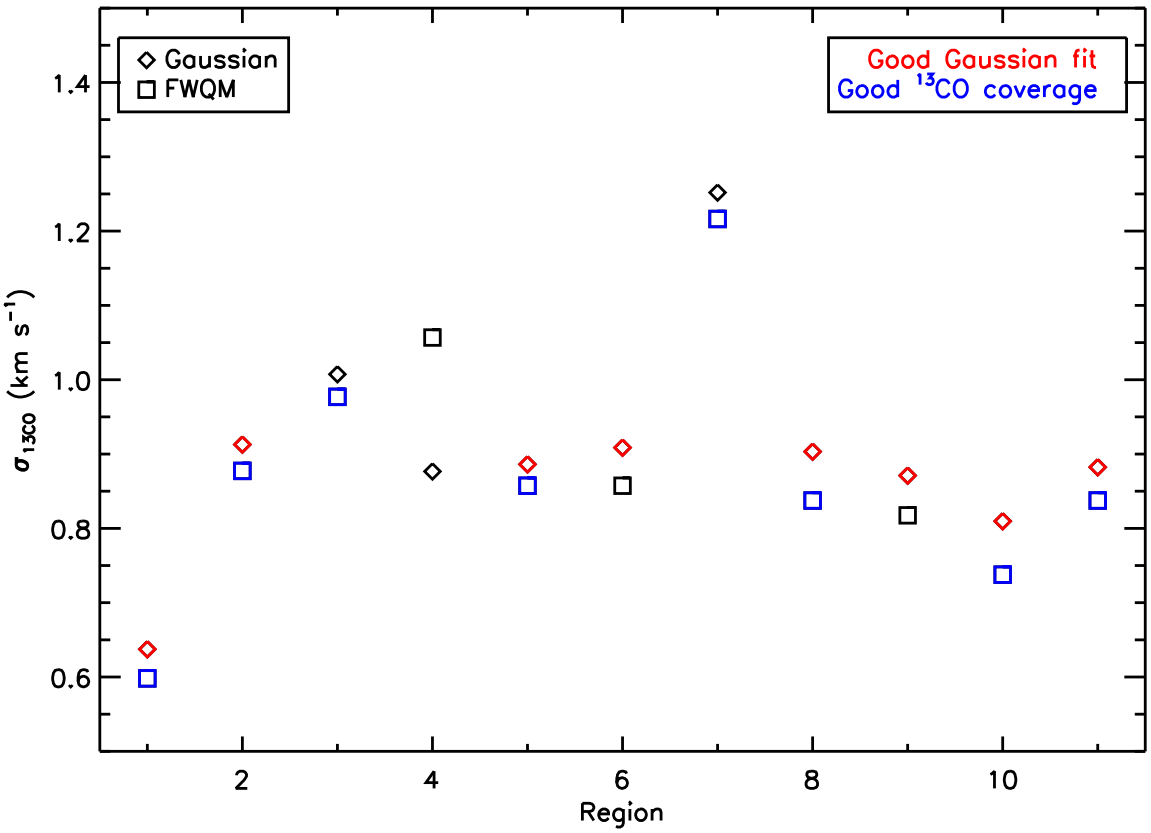

Fig. 4.— A comparison of the different measures of the velocity dispersion within each extinction region, illustrating that the measures are similar in regions where the ^{13}CO coverage is good. The ^{13}CO velocity dispersion is measured with both a single Gaussian (diamonds) and the equivalent Gaussian sigma derived from measuring the full width at quarter maximum (FWQM) of the spectra (squares). Red points denote the single Gaussian fits that were judged by eye to fit well, while blue points denote regions where the ^{13}CO data covers 80% or more of the extinction region, i.e., the spectrum is a good representation of that for the entire region. In all regions where there is good ^{13}CO coverage (blue points), both velocity dispersion measurements (diamonds and squares) are similar, regardless of whether the single Gaussian fits were judged to be good (red points) or not. The remainder of this paper uses the single Gaussian fit measures, restricted to regions where there is good ^{13}CO coverage.

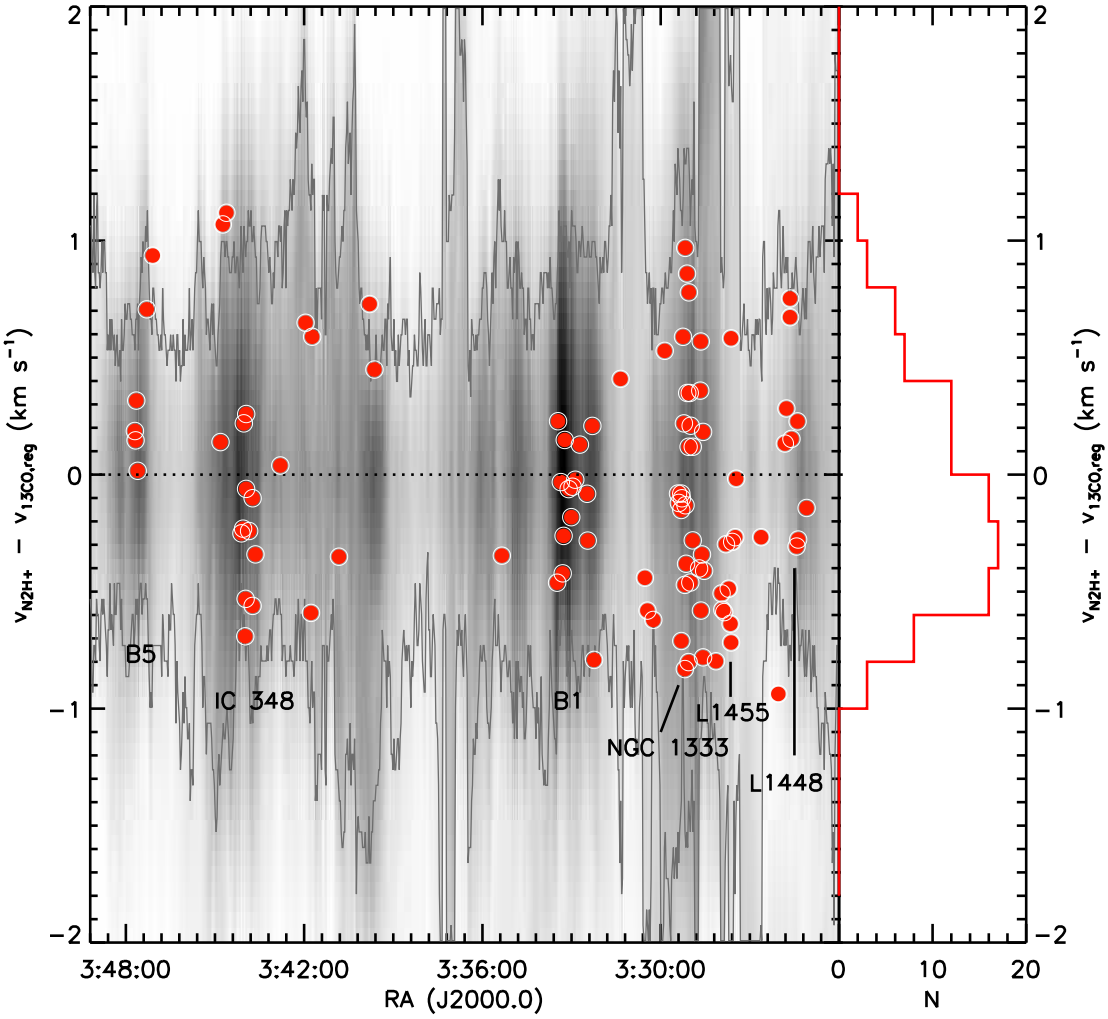

Fig. 5.— The distribution of the centroid velocity difference between N_2H^+ and the ^{13}CO region in which the core is located as a function of RA (left panel), and the total distribution (right panel). The greyscale image in the left panel shows the position-velocity (PV) diagram for the ^{13}CO gas with the grey contours showing the half-maximum value at every RA. At each RA, the cumulative spectrum has been shifed so that the peak intensity falls at a value of zero on the diagram. The greyscale ranges from 2 K km s^{-1} (black) to 0 K km s^{-1} (white).

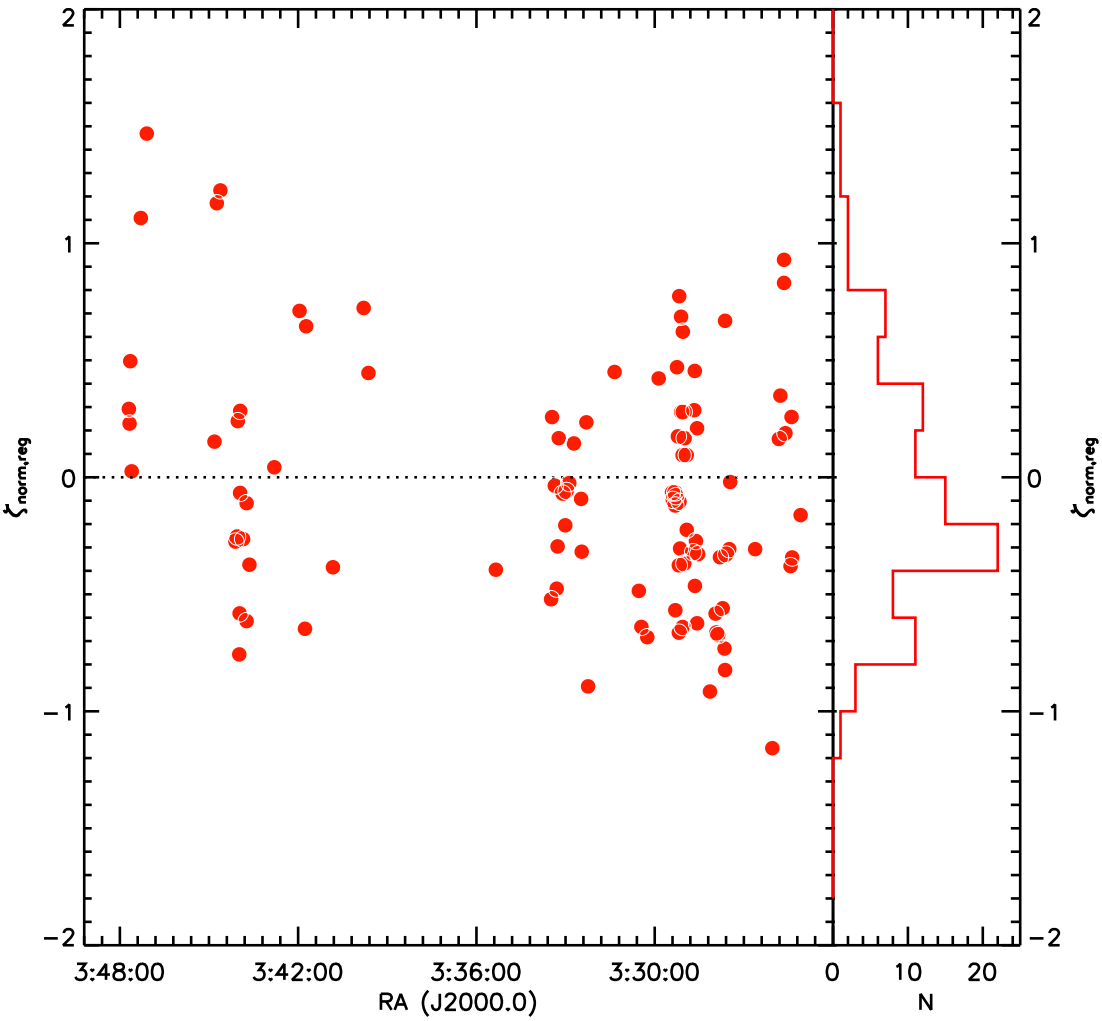

Fig. 6.— The distribution of normalized centroid velocity differences, ζ_{norm} between the N_2H^+ and the region in which the core is located as a function of RA (left panel) and the total distribution (right panel). See previous figure for the plotting conventions used.

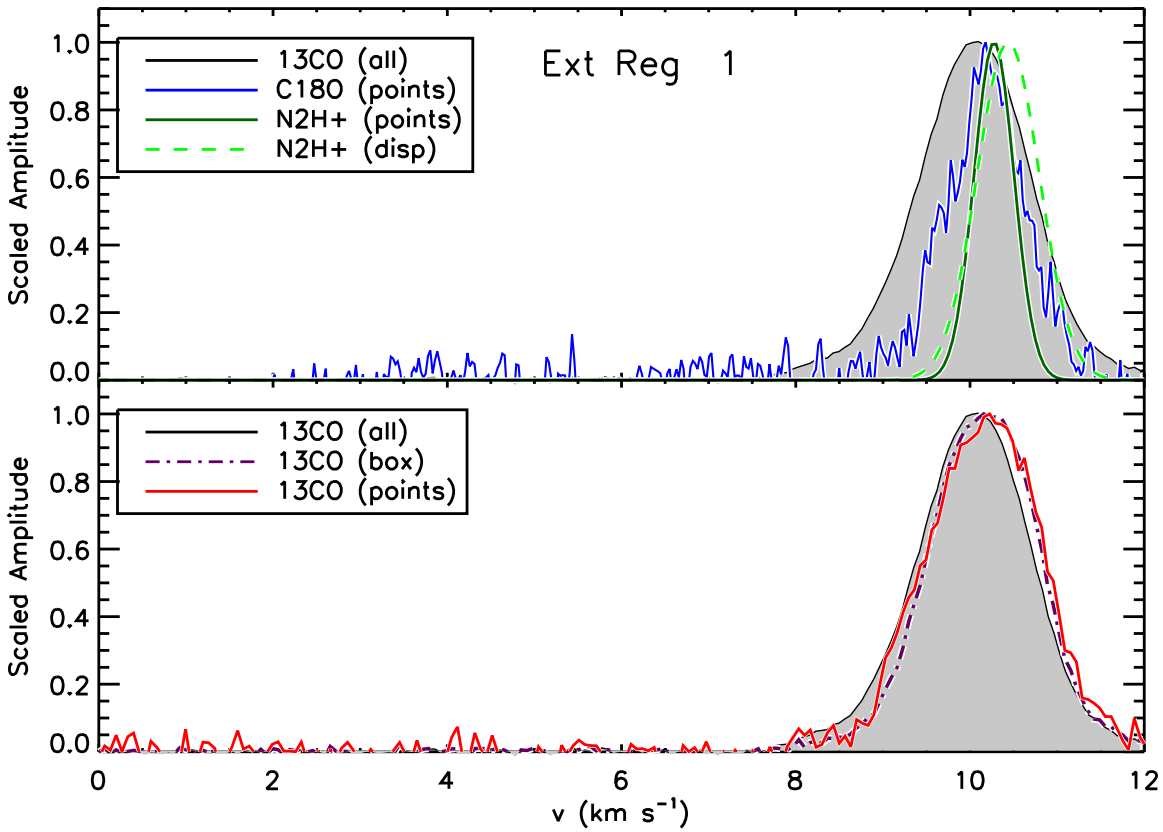

Fig. 7.— A comparison of cumulative spectra within extinction region 1. Top panel: The ^{13}CO spectrum of the entire region from the top panel (black line and grey shading), the C^{18}O spectrum summed over all locations in the region with C^{18}O detections ("method B", blue line), the resultant fit for a similar summation for N_2H^+ ("method B", dark green line), and the standard deviation of the centroid N_2H^+ velocities in each region ("method A"), centered on the mean value (light green dashed line). Bottom panel: ^{13}CO spectra derived from summing the spectra over the entire region (black line), summing over the box in which the N_2H^+ dense cores are found only (purple dot-dashed line), and summing over only the points where where N_2H^+ dense cores were detected (red line). Note the ^{13}CO spectral data has a full range of ~ -10 to 30 km s^{-1}; the truncated range of 0 to 12 km s^{-1} plotted covers the range of velocities where N_2H^+ and C^{18}O emission was observed.

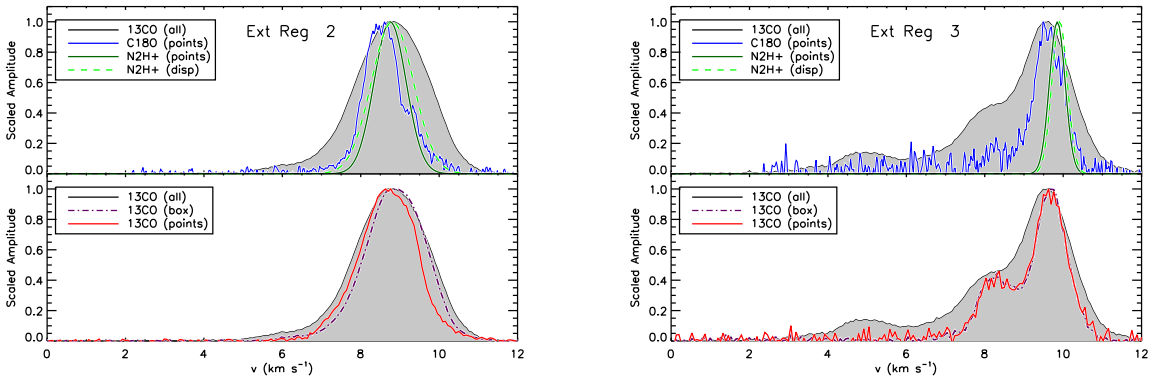

Fig. 8.— Cumulative spectra within extinction regions 2 and 3. See Figure 7 for the plotting conventions used.

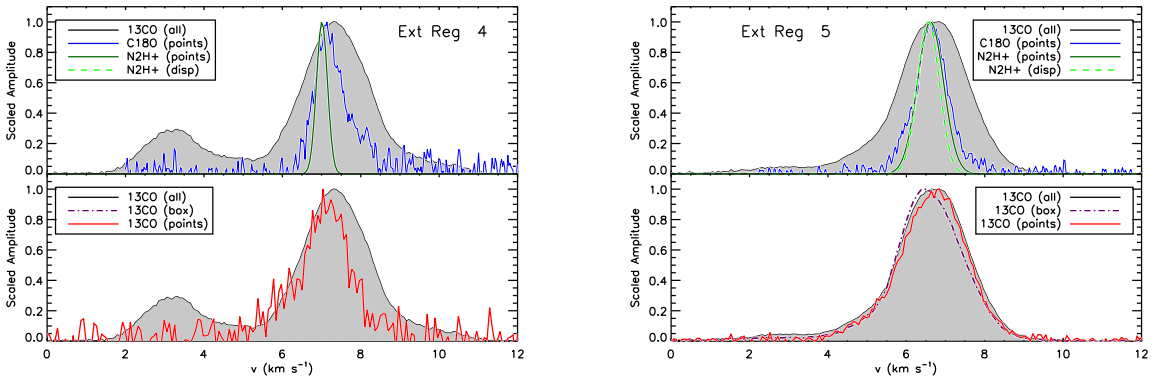

Fig. 9.— Cumulative spectra within extinction regions 4 and 5. See Figure 7 for the plotting conventions used. Note that in extinction region 4, only one dense core was observed, so the standard deviation of N_2H^+ centroid velocities (dashed green line) cannot be plotted in the top panel. The purple dashed and red solid line are identical in the bottom plot for the same reason.

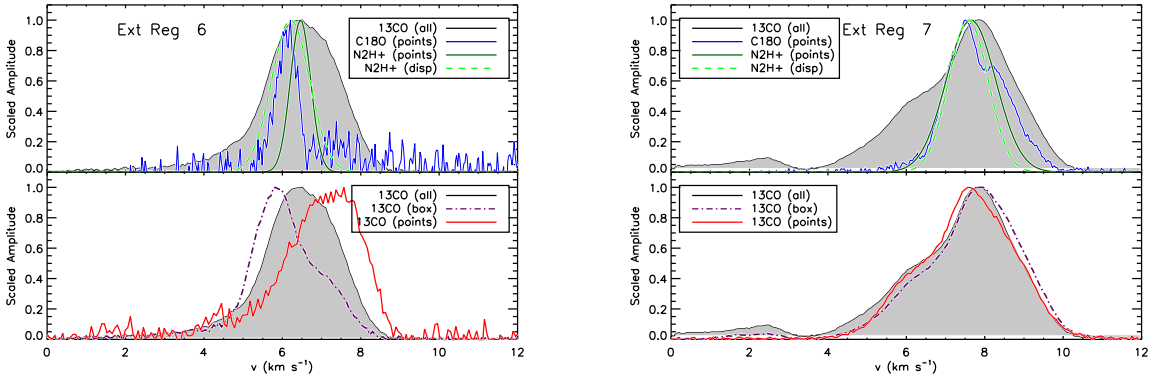

Fig. 10.— Cumulative spectra within extinction regions 6 and 7. See Figure 7 for the plotting conventions used. The offset in N_2H^+ centroids in extinction region 6 is caused by the small number of cores (four) in the region, one of which is faint enough that it impacts the measurement using method A only.

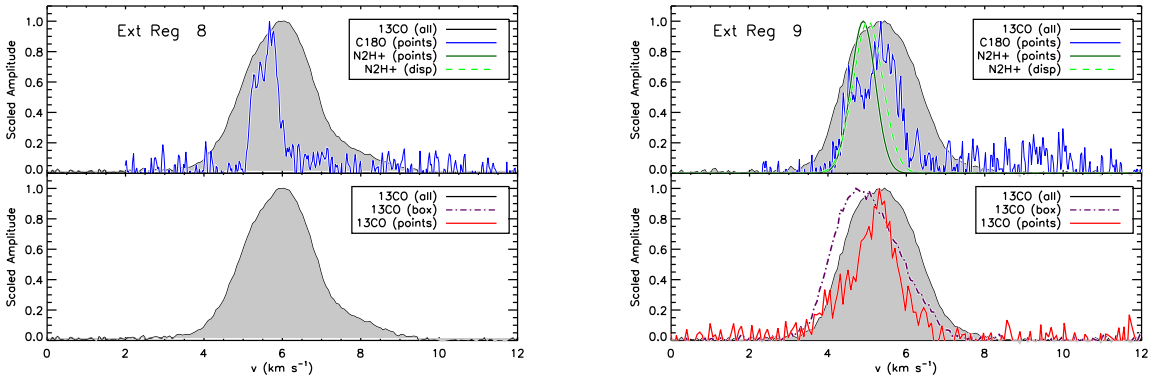

Fig. 11.— Cumulative spectra within extinction regions 8 and 9. See Figure 7 for the plotting conventions used. Note that there were no N_2H^+ detections in extinction region 8.

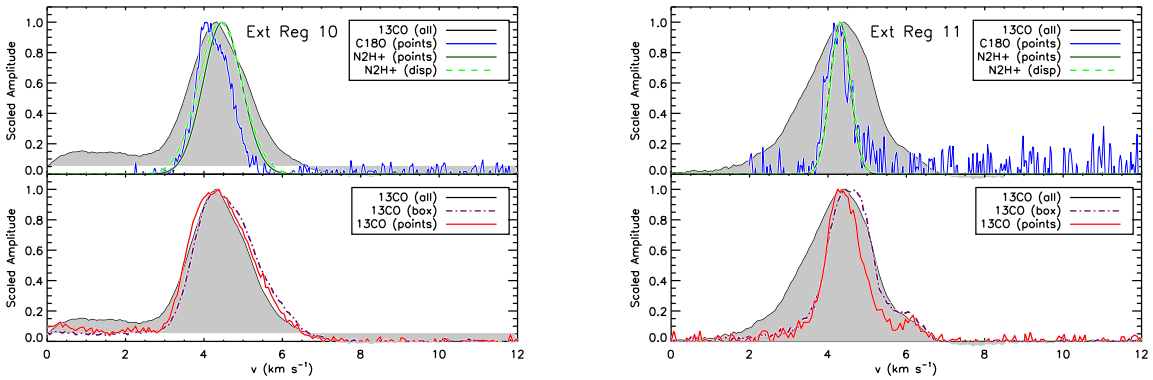

Fig. 12.— Cumulative spectra within extinction regions 10 and 11. See Figure 7 for the plotting conventions used.

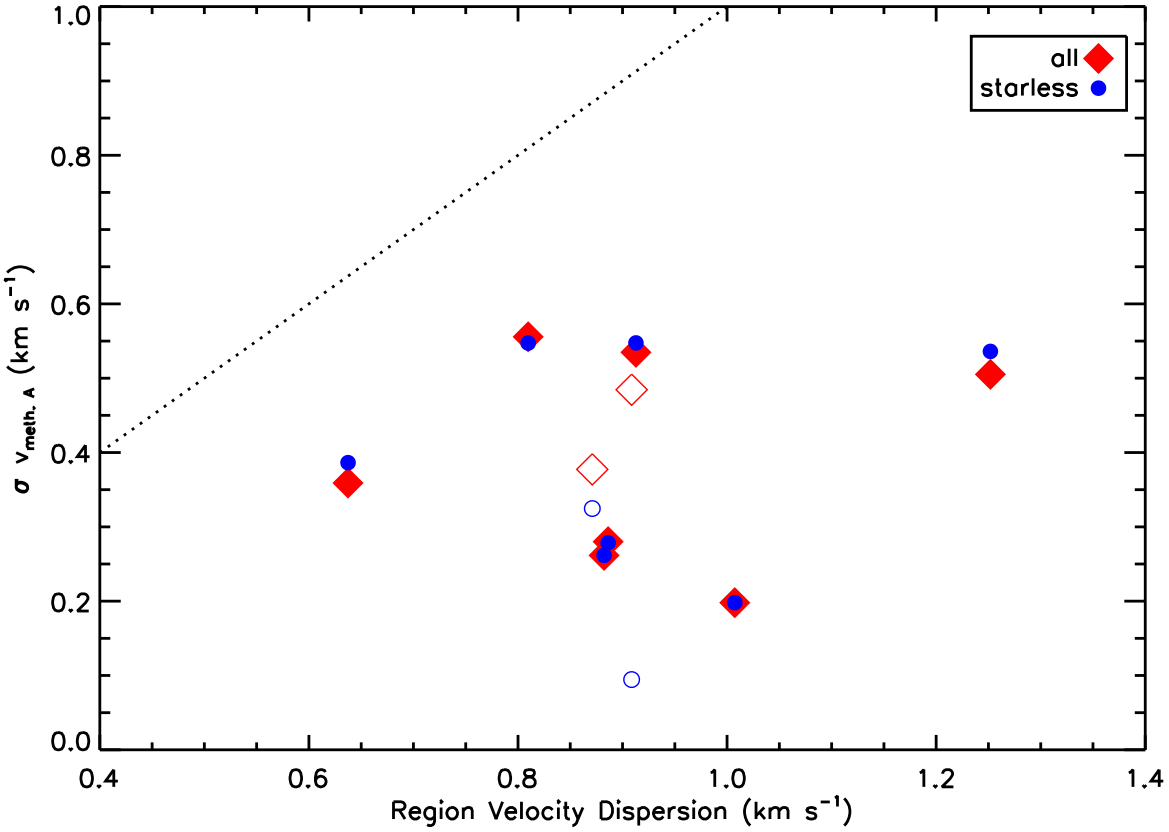

Fig. 13.— The spread in core-to-core velocity dispersions found in each extinction region versus the velocity dispersion of that region. The diamonds show the values derived using all of the dense cores within each region, while the circles show the values derived using only the starless cores within each region. The open symbols denote the values derived for the extinction regions with poor ^{13}CO coverage. The dotted line shows a 1-1 relationship.

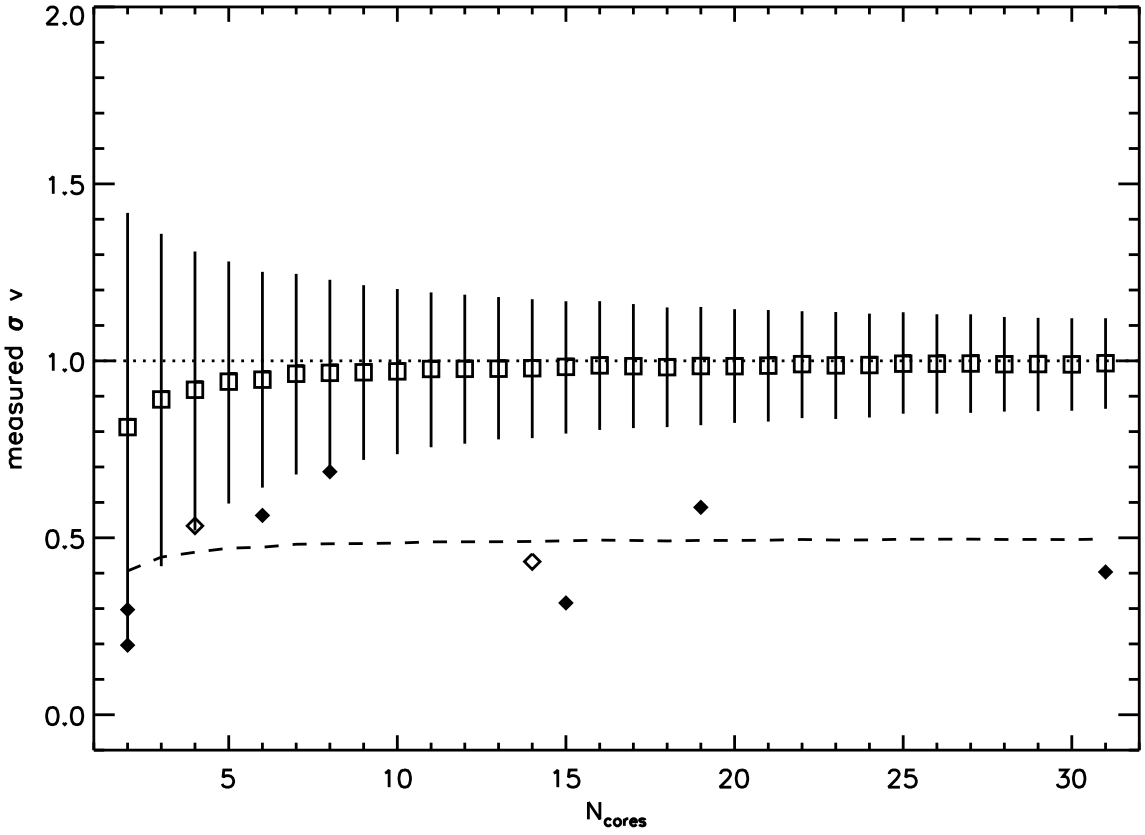

Fig. 14.— The expected range of observed core-to-core velocity dispersions relative to the distribution they were drawn from for a given number of cores. The boxes and vertical lines show the scaled mean and standard deviation of the core-to-core velocity dispersion for varying numbers of cores observed. The diamonds show our observed values scaled to the velocity dispersion of the region, with the open symbols denoting the extinction regions with poor ^{13}CO coverage. The dotted horizontal line indicates an observed velocity dispersion equal to that of the parent sample, while the dashed line shows the scaled mean core-to-core velocity dispersion values multiplied by one half.

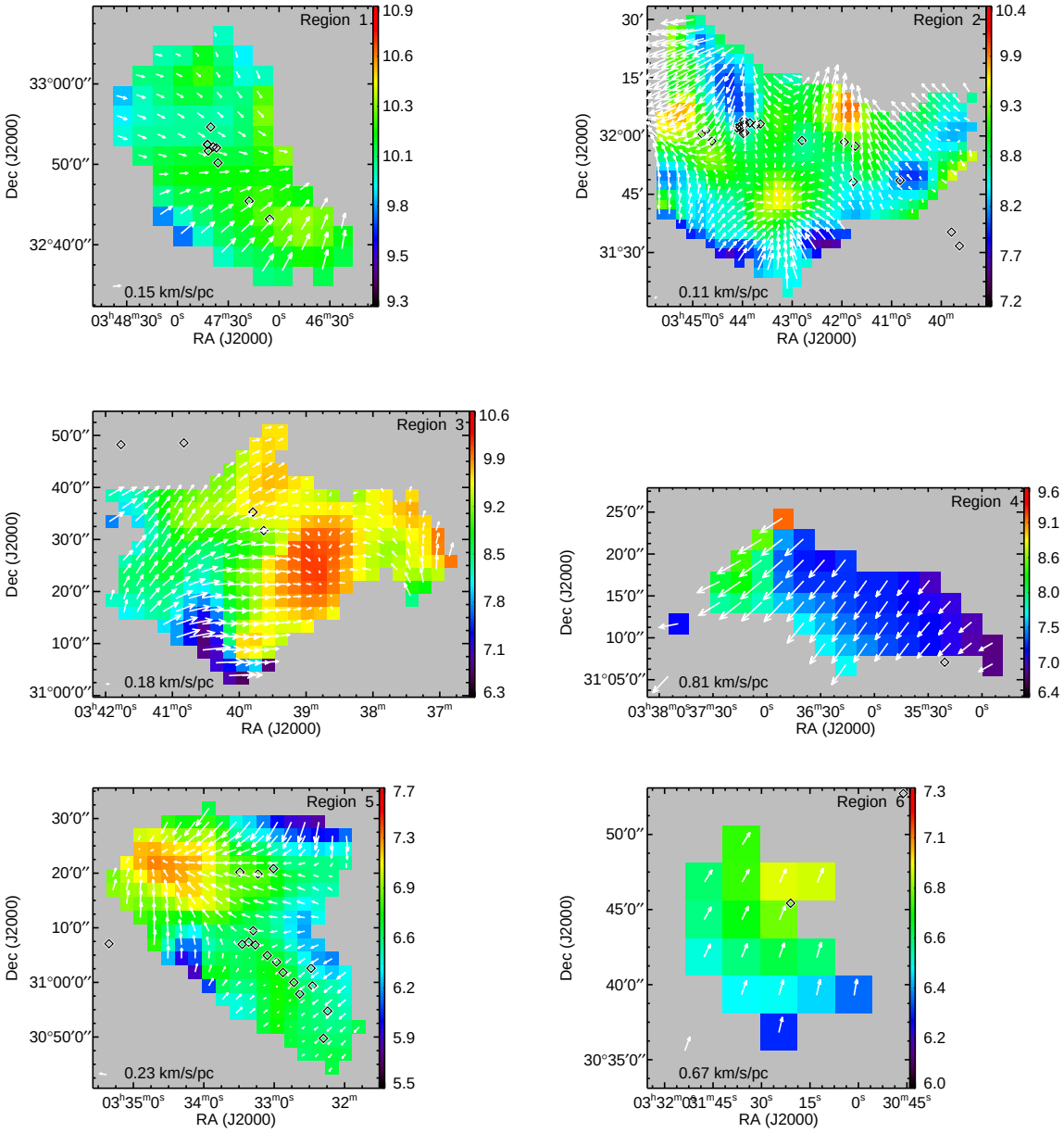

Fig. 15.— The overall velocity gradient measured for each extinction region in ^{13}CO for extinction regions 1-6. The colourscale indicates the centroid velocity of each cell, while the arrows indicate the direction of the local gradient. The overall gradient is indicated in the bottom left corner of each panel. Diamonds show the positions of the N_2H^+ cores in each region.

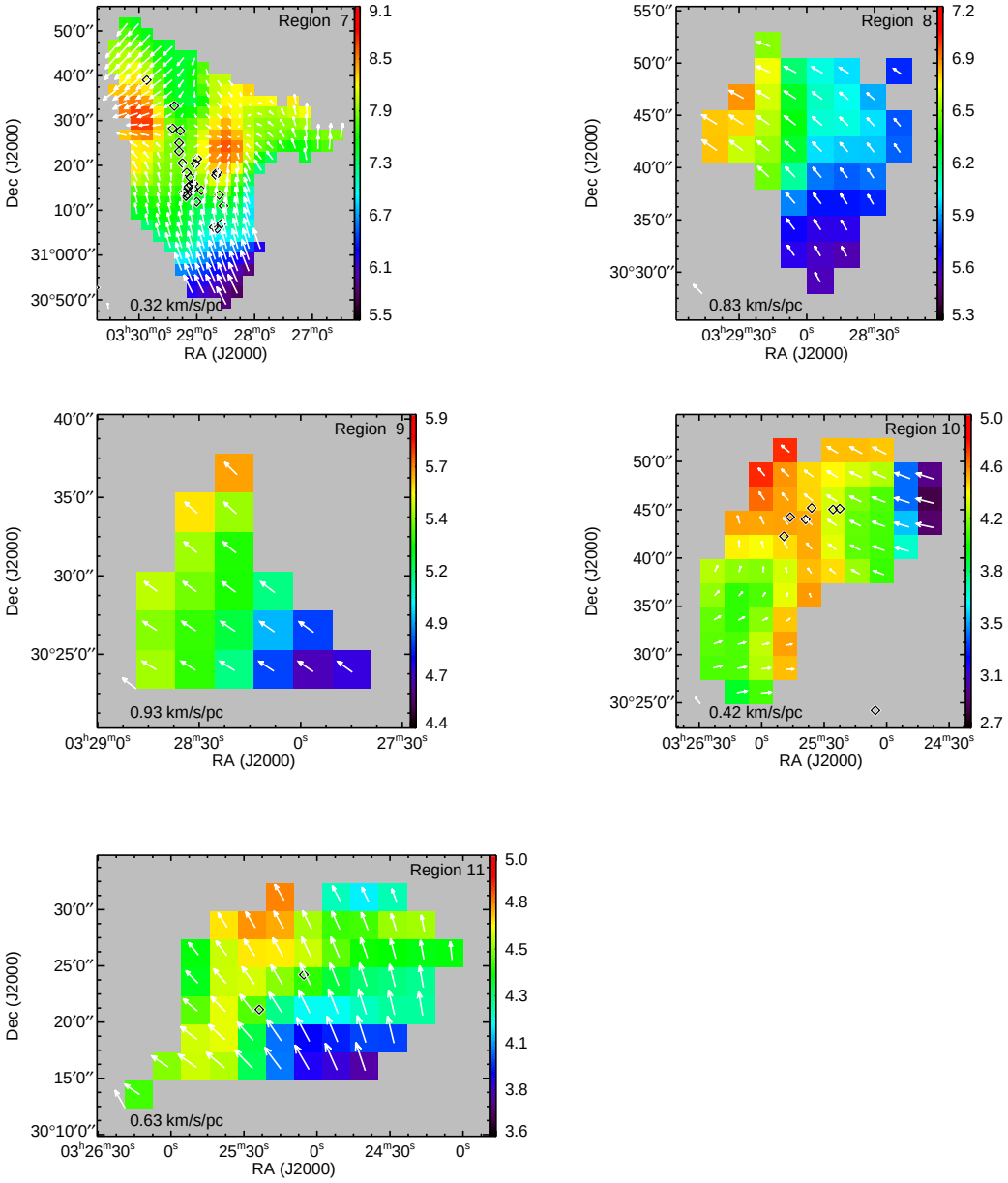

Fig. 16.— The overall velocity gradient measured for each extinction region in ^{13}CO for extinction regions 7 to 11. The colourscale indicates the centroid velocity of each cell, while the arrows indicate the direction of the local gradient. The overall gradient is indicated in the bottom left corner of each panel. Diamonds show the positions of the N_2H^+ cores in each region.

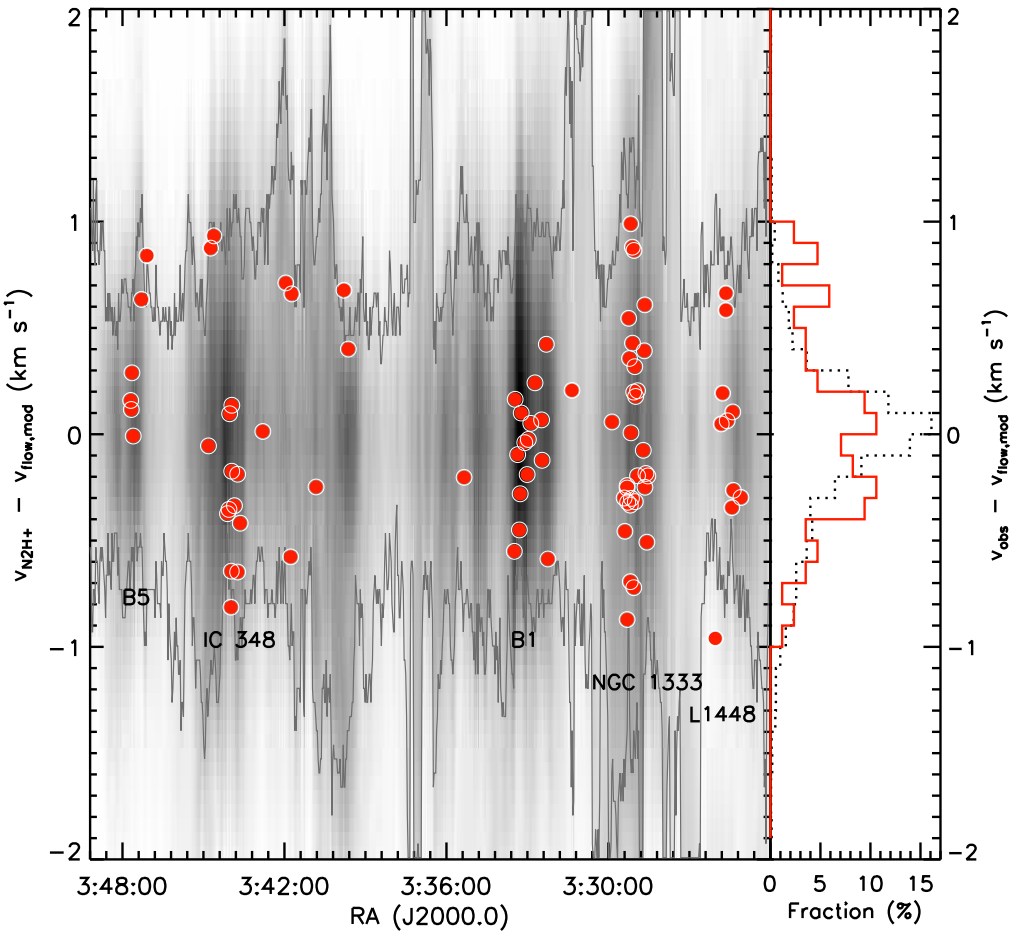

Fig. 17.— The distribution of centroid velocity differences between the dense cores and the velocity inferred at their location from the ^{13}CO velocity gradient measured in their extinction region (points) as a function of RA (left panel). The RAs of well-known star-forming regions are noted, with the exception of L1455 where the ^{13}CO observations do not cover a large enough area to allow for a model of the gradient to be applied. As in Figure 2, the background greyscale image shows the PV diagram of the ^{13}CO gas and the grey contours show the half-maximum value at every RA, with the spectrum at each RA shifted so that the peak emission falls at 0. The total distrbution of $v_{N2H+} - v_{flow,mod}$ is shown in the right panel in red, and for comparison, the total distribution of $v_{13CO} - v_{flow,mod}$ is shown in black.

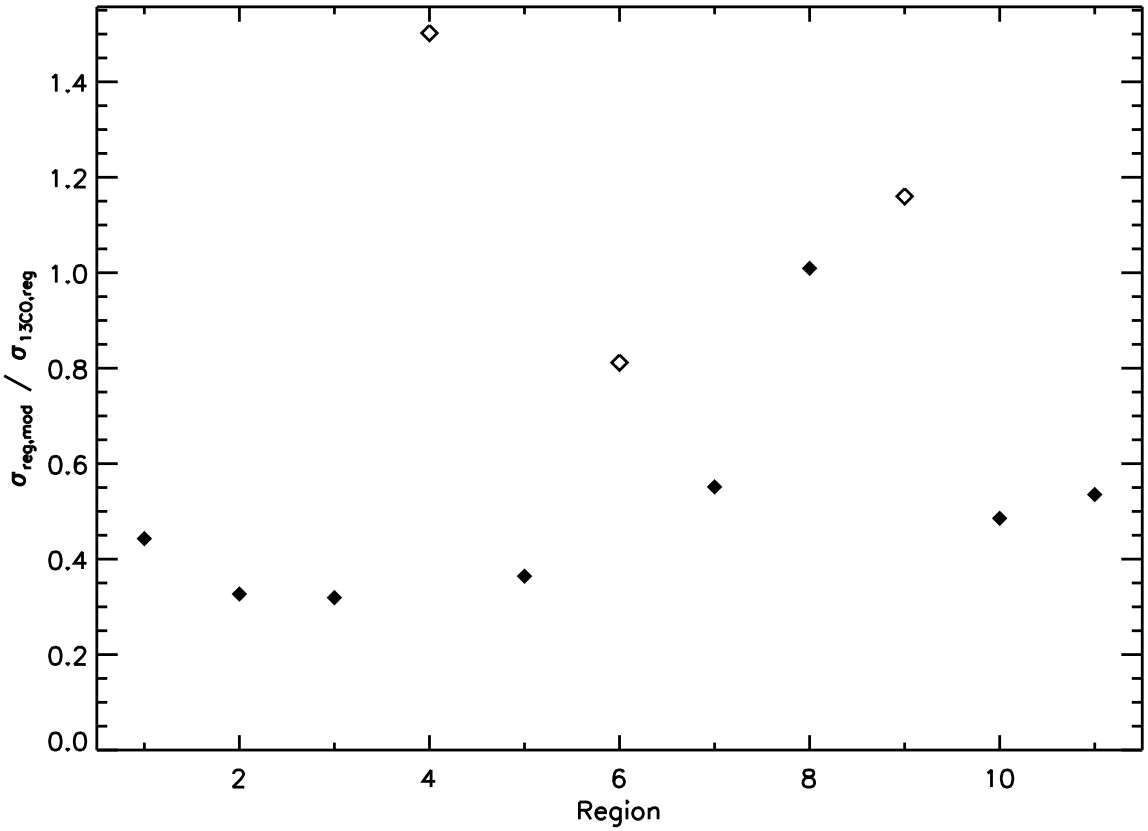

Fig. 18.— The ratio of large-scale to total velocity dispersion observed in each extinction region. The open symbols show the results for the three extinction regions where the ^{13}CO coverage is less than 80% and hence less reliable.

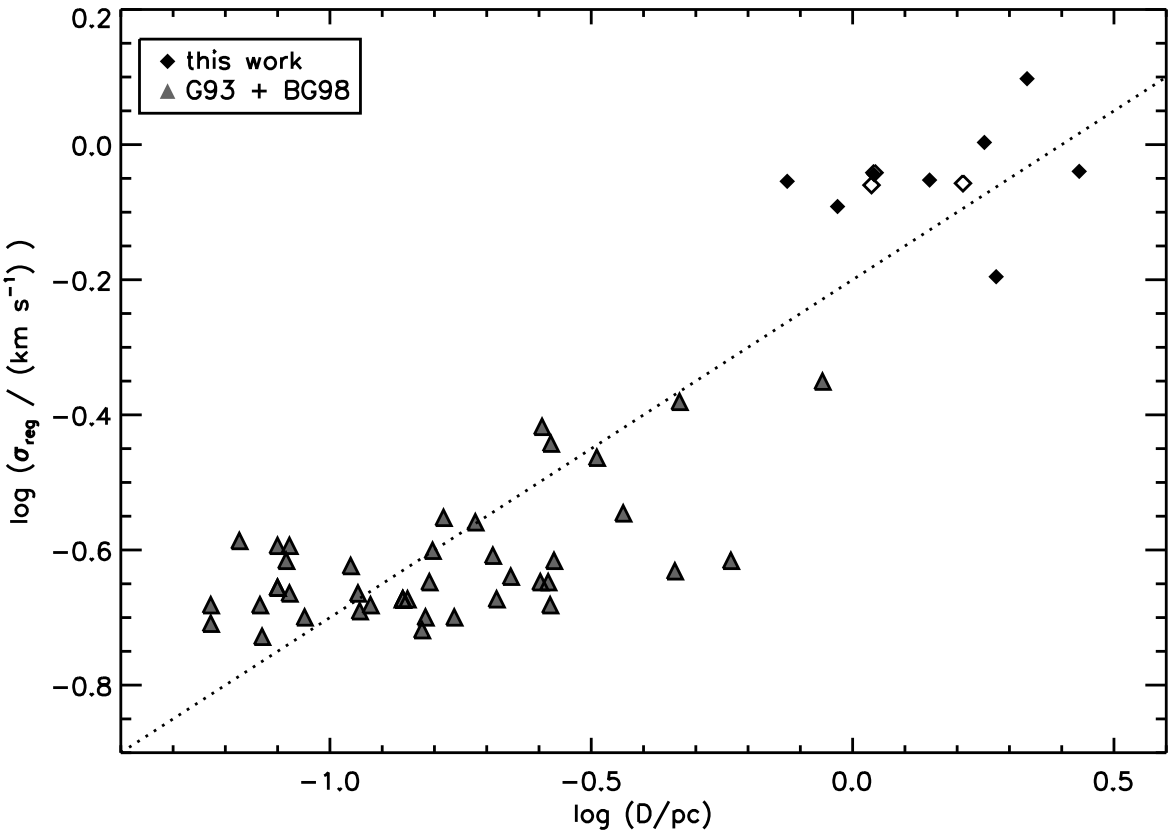

Fig. 19.— The observed velocity dispersion versus diameter for all of the extinction regions (diamonds) and NH_3 cores in Goodman et al. (1993) (triangles). The open symbols show the results for the regions where the ^{13}CO coverage was less than 80%. The dotted line shows the slope of the scaling relationship assumed by Burkert & Bodenheimer (2000), $\sigma \propto R^{0.5}$. Note that a scale factor for the relationship is not given in Burkert & Bodenheimer (2000), so the line plotted is a guide to the slope only.

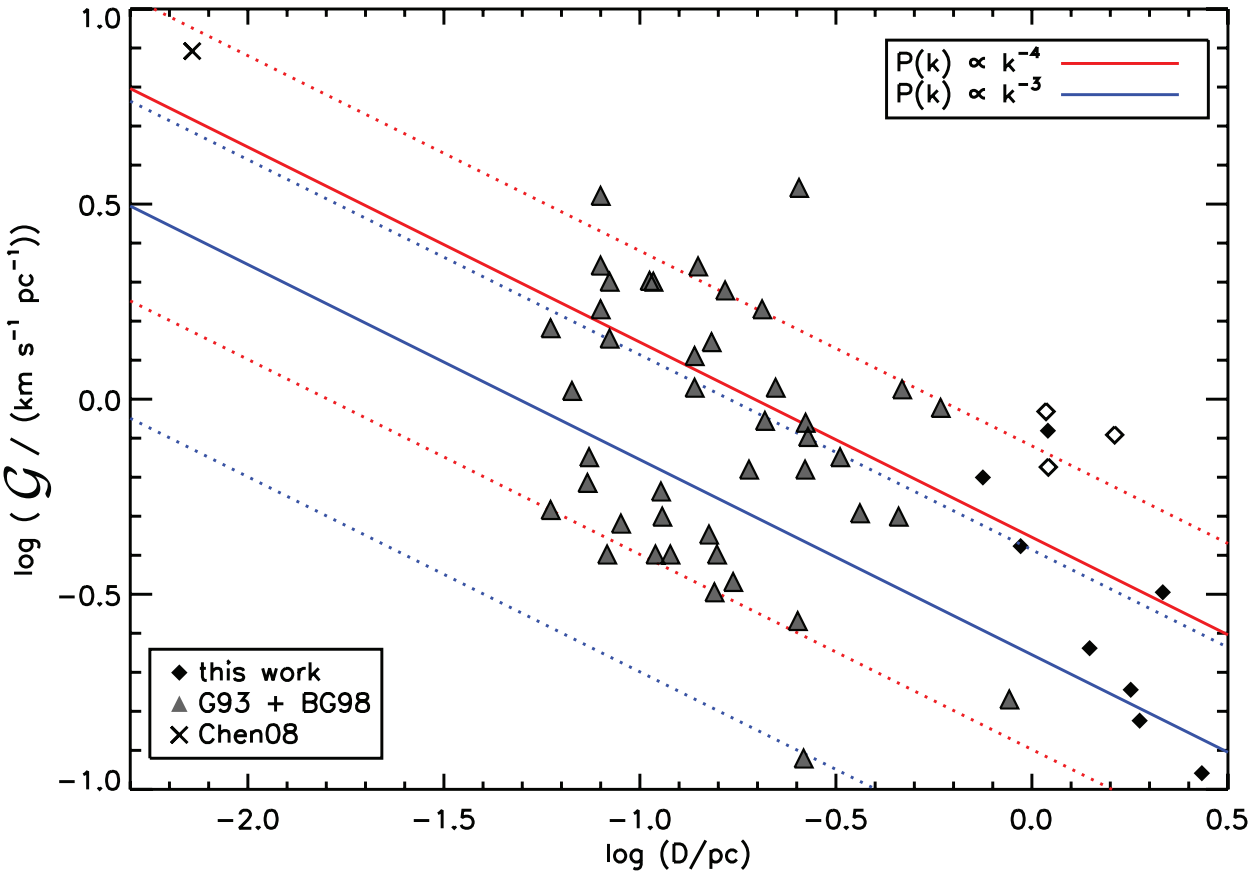

Fig. 20.— The gradient measured for each extinction region versus the diameter of the region (diamonds). The open diamonds show the results for the three extinction regions where the ^{13}CO coverage was less than 80% and hence less reliable. The triangles show the data from the NH_3 cores of Goodman et al. (1993), while the cross shows data from Chen et al. (2008); see text for details. The red diagonal lines show the range (dotted) and most likely values (solid) predicted by BB00 for a k^{-4} turbulent power spectrum, while the blue lines show the range (dotted) and most likely values (solid) for a k^{-3} turbulent power spectrum.